

University of Nevada, Reno

**A New Data Processing System for Generating Sea Ice Surface Roughness and
Cloud Mask Data Products from the Multi-Angle Imaging SpectroRadiometer
(MISR)**

A dissertation submitted in partial fulfillment of the
requirements for the degree of Doctor of Philosophy in
Atmospheric Science

by

Ehsan Mosadegh

Dr. Anne W. Nolin/ Dissertation Advisor

May 2023

© by Ehsan Mosadegh 2023

All Rights Reserved



THE GRADUATE SCHOOL

We recommend that the dissertation
prepared under our supervision by

EHSAN MOSADEGH ANBARAN

entitled

**A New Data Processing System for Generating Sea Ice Surface
Roughness and Cloud Mask Data Products from the Multi-Angle
Imaging SpectroRadiometer (MISR)**

be accepted in partial fulfillment of the
requirements for the degree of

DOCTOR OF PHILOSOPHY

Anne W. Nolin, Ph.D.

Advisor

Vera Samburova, Ph.D.

Committee Member

Eric Wilcox, Ph.D.

Committee Member

Feng Yan, Ph.D.

Committee Member

Thomas P. Albright, Ph.D.

Graduate School Representative

Markus Kemmelmeier, Ph.D., Dean

Graduate School

May-2023

Abstract

This study describes two novel data products derived from Multi-angle Imaging SpectroRadiometer (MISR) imagery: Arctic-wide maps of sea ice roughness and a binary cloud detection algorithm. The sea ice roughness maps were generated using a data processing system that matched MISR pixels with co-located and concurrent lidar-derived roughness measurements from Airborne Topographic Mapper (ATM), calibrated the multi-angle data to values of surface roughness using a K-Nearest Neighbor (KNN) algorithm, and then applied the algorithm to Arctic-wide MISR data for two 16-day periods in April and July 2016. The resulting maps show good agreement with independent ATM roughness data and enable characterization of the roughness of different ice types. The binary cloud detection algorithm was developed using a neural network approach and a training dataset constructed from Top-of-Atmosphere red band values from all MISR's nine different viewing cameras for the same two months in various regions of the Arctic. The algorithm showed good performance in classifying pixels into cloudy and clear categories in MISR images, with better performance for clear pixels in April 2016 and better performance for cloudy pixels in July 2016. The algorithm also provides a significant advantage over existing MISR cloud mask products SDCM and ASCM in terms of accuracy and spatial resolution, with a resolution of 275 meters. The data products presented here can be used to gain insights into the seasonal and interannual changes in sea ice roughness and cloud cover over the Arctic and to develop and improve more accurate classification algorithms in the field of remote sensing.

I dedicate my doctorate dissertation to my beloved family, especially to my father and mother for their constant support and unconditional love.

There are no words to convey how much I love you.

Acknowledgments

I greatly thank my Ph.D. research advisor, Professor Anne W. Nolin, for her scientific advice and many insightful discussions and suggestions. She gave me the freedom and support to develop independent research ideas. I am thankful for her guidance, for being so available for her students, and for providing me the opportunity to learn machine-learning techniques and explore their applications in remote sensing observations. I appreciate her sharp perspectives, superb knowledge of science, and positive attitude especially when facing difficulties. I have been extremely lucky to have such an advisor.

I also wish to thank the members of my Ph.D. committee, Professors Eric Wilcox, Vera Samburova, Feng Yan, and Thomas P. Albright for their knowledge and scientific advice during my graduate school and their constructive comments that helped to improve my research work.

Also, I wish to thank NASA-JPL for supporting this research work through their generous grant. A general thanks to NASA for advanced technologies and numerous open-access satellite data for research purposes.

Sincere thanks to all of my colleagues at Desert Research Institute (DRI) and the University of Nevada Reno (UNR), especially Dr. Vera Samburova, the director of the Atmospheric Sciences Graduate Program at DRI, for their support and help during my Ph.D. career. I am happy I had this opportunity to collaborate with research groups and academic faculty members at the DRI and the UNR.

I am thankful for the support of my friends. Special thanks to Dr. Iman Babaeian for his encouragement and support from overseas. I thank Marco Giordano and Mohammad Sadrian for their encouragement during my Ph.D. journey.

And I deeply thank my wonderful family for the love, support, and encouragement they have given me along this journey. My hard-working parents have provided unconditional love and support and I would not have made it this far without them. Furthermore, I thank my wonderful brothers, Ali and Iman, for all their support in my Ph.D. journey.

Table of Contents

Abstract.....	i
Acknowledgments.....	iii
Chapter 1.....	1
Introduction.....	1
Chapter 2.....	13
A New Data Processing System for Generating Sea Ice Surface Roughness Products from the Multi-angle Imaging SpectroRadiometer (MISR) Imagery.....	13
Abstract.....	14
2. Methods.....	18
3. Results.....	26
4. Discussion.....	40
5. Conclusion.....	43
Chapter 3.....	46
Development and Evaluation of a Neural Network-based Cloud Detection Algorithm for Multi-Angle Imaging SpectroRadiometer (MISR) Imagery.....	46
Abstract.....	47
1. Introduction.....	48
2. Methodology.....	53
3. Results.....	60
4. Discussion and Conclusion.....	68
Chapter 4.....	73
Summary and Conclusions.....	73
References.....	79

List of Tables

Table 1. Remote sensing of some important processes and characteristics of sea ice.....	5
Table 2. Statistics of sea ice roughness model performance.	27
Table 3. Confusion matrix for April 2016.....	62
Table 4. Confusion matrix for July 2016.	62
Table 5. Performance statistics for April 2016.....	63
Table 6. Performance statistics for July 2016.	63

List of Figures

Figure 1. Data processing steps.	25
Figure 2. Histograms comparing MISR-estimated (using the KNN model) and ATM-observed (independent test data) sea ice roughness for (a) April and (b) July 2016. The brown color is where the blue and orange colors overlay each other.	29
Figure 3. Q-Q plots for the April and July 2016 datasets (a and b) show the error distribution of MISR-estimated roughness for (a) April and (b) July 2016.....	30
Figure 4. Spatial patterns of mean sea ice surface roughness derived from MISR images (275 m resolution) over the Arctic region for 16-day periods of (a) 15–30 April 2016 and (b) 10–25 July 2016.	32
Figure 5. Mean MISR-derived sea ice surface roughness for two locations: the Arctic Ocean (AO) north of the Canadian Archipelago, and Fram Strait (FS) east of Greenland. (a) the AO in spring, (b) the AO in summer, (c) FS in spring, and (d) FS in summer.	34
Figure 6. Comparison of (a) MISR-derived roughness map with (b) Landsat 8 and (c) Sentinel-1 images at an arbitrary location north of the Canadian Archipelago on 29 April 2016 at 116.1 W and 77.5 N.....	37
Figure 7. Comparison of (a) MISR-derived roughness map with (b) Landsat 8 for July 20th and (c) Sentinel-1 for July 19th images at an arbitrary location at the Fram Strait in July 2016 at 18.7 W and 76.5 N.....	38
Figure 8. Comparison of (a) MISR-derived roughness map with (b) Landsat 8 for the ice-free area around the Zemlya George archipelago for a cloud-free period from 10–15 July 2016. Dark-blue patches in our MISR-derived map are the Zemlya George island.....	42
Figure 9. The architecture of the developed neural network model for both seasons. The algorithm has 3 dense layers and 9 nodes at its input layer. From left to right, there are 64, 32, and 2 neurons in each hidden layer. The network has 2 output nodes that represent 2 classes, clear and cloudy.	61
Figure 10. Grayscale image of a cloudy image.....	67
Figure 11. False color composite R(Ca) G(An) B(Cf) image of a cloudy block.	67
Figure 12. In the ASCM cloud mask, blue is clear HC, and white is cloudy HC.....	67
Figure 13. In the NNCM cloud mask, blue is clear, and white is cloudy.	68

Chapter 1

Introduction

Sea ice is an important part of the Earth's climate system and is one of the fastest-changing elements in response to climate warming (Mueller et al., 2018; Notz and Community, 2020; Rantanen et al., 2022; Stroeve and Notz, 2015). The abrupt reductions in Arctic summer sea-ice extent and concentration over the past few decades are common insights from remote sensing observations and model reanalysis simulations (Kumar et al., 2020; Kwok and Rothrock, 2009; Meier et al., 2007; Stroeve and Notz, 2018). These events are characterized by decreasing ice extent trends with the highest decline in September (Holland et al., 2006). Satellite observations indicate a 40% decline in thickness, primarily due to the loss of thicker, older ice cover (Meier et al., 2014). The changes are happening faster than models have projected, and summer ice-free conditions are likely in the coming decades (Meier et al., 2014). The changes in Arctic sea ice contribute to the ice-albedo feedback (Landy et al., 2015) and are already affecting flora, fauna, and people living in the Arctic, with some species facing challenges while new habitat opens up. Despite progress, significant challenges remain in understanding the processes, impacts, and future evolution of the system.

Surface roughness is a geophysical property and a component of surface topography. Surface roughness is linked to variations in surface topography and can be defined as the deviations of measured surface elevations from a reference surface. Sea ice surface

roughness can be used to characterize important physical properties of sea ice and is often a good prognostic variable of sea ice properties such as ice thickness, ice age, melt pond extent, and ice-albedo feedback (Landy et al., 2015). Surface roughness can modulate Arctic processes across various scales and plays an important role in Arctic planetary boundary layer processes.

The surface roughness of ice plays an important role in the evolution of the Arctic sea ice cover. Melt pond formation plays an important role in the energy balance of the region in that liquid water on the ice surface dramatically decreases the ice surface albedo. Summer melt pond fraction, which quantifies the spatial coverage of meltwater on the ice surface, is one key parameter that has been related to sea ice surface roughness (Landy et al., 2015). During the melt season, the crevices found in rough ice constrain the meltwater extent, while smoother sea ice enhances the spread of meltwater over the surface. Thus, melt pond extent is greater over smoother first-year ice compared with rougher, multi-year sea ice (Landy et al., 2015; Zhang et al., 2000).

Melt pond coverage on the ice surface is governed by local ice surface topography which is often governed by ice type (Eicken et al., 2004; Fetterer and Untersteiner, 1998; Morassutti and Ledrew, 1996). Furthermore, ice topography significantly impacts planetary boundary layer processes such as turbulent fluxes of momentum (drag) and sensible/latent heat over the ice surface (Arya, 1973; Steiner et al., 1999). These boundary layer processes can be linked to the surface topography through aerodynamic roughness length and drag coefficients. On the other hand, surface momentum exchange is sensitive to sea ice concentration and morphology (Elvidge et al., 2015). Therefore, sea ice surface

roughness modulates turbulent momentum flux between the Earth's surface and the atmosphere (Petty et al., 2017; Steiner et al., 1999). A rougher surface increases surface stress and it produces larger turbulent eddies due to increased surface roughness (Arya, 1973, 1975; Petty et al., 2017).

A detailed representation of atmospheric momentum fluxes can help us better understand the dynamic coupling in the ice-ocean-atmosphere system. Over the polar oceans, sea-ice surface topography strongly influences near-surface atmospheric transport of momentum and in some Arctic regions, the largest impact on drag coefficients is due to minor surface roughness elements rather than large topographic features such as pressure ridges (Castellani et al., 2014). On the other hand, sea ice surface topography has spatial and temporal variations and this will reflect in spatial and temporal variability of aerodynamic roughness length and drag coefficients (Castellani et al., 2014; Petty et al., 2017). The surface roughness of sea ice and the ice sheet is parameterized in numerical atmospheric and climate models and is modeled as a constant value over large spatial domains. However, aerodynamic roughness length has high spatiotemporal variability over the Arctic (van Tiggelen et al., 2021). Therefore, more precise estimates of surface roughness can benefit the development of models and algorithms.

Moreover, surface roughness is closely related to ice thickness (Peterson et al., 2008). There is a linkage between sea ice surface roughness and ice dynamics such as divergence and convergence processes that influence the motion of sea ice. Ice dynamics is considered a source of variability in the Arctic Ocean ice thickness (Kwok, 2015). Sea ice convergence results in ridges and ultimately contributes to the formation of thicker, multiyear ice cover.

These ridges will increase the roughness of the sea ice surface, will affect the backscattering properties of sea ice, will reduce melt pond coverage formed in the melt season, and consequently will reduce ice loss due to the decrease in sea ice surface insolation (Kwok, 2015). We need to acquire more observations of parameters such as sea ice roughness to fully understand the effect of ice convergence on summer ice extent.

Moreover, sea ice morphology influences surface roughness (Elvidge et al., 2015), and surface roughness of the ice plays an important role in the evolution of the ice cover through positive albedo feedback loop mechanisms enhanced by fracturing and meltwater pond formation of sea ice (Lindsay and Zhang, 2005; Moritz et al., 2002; Stroeve et al., 2012; Zhang et al., 2000). Ice surface roughness can be related to ice cover evolution through the important role of melt pond coverage that will change the ice surface albedo (Landy et al., 2015; Zhang et al., 2000).

As such, sea ice roughness can be considered a useful proxy for several sea ice characteristics and parameters such as sea ice thickness, age, type, and surface albedo. Also, it is important to be able to expand the modeling analyses to larger spatial and temporal scales, because monitoring and retrieving a better estimate of sea ice roughness will help us better understand polar ecosystems which can provide us more insight into global climate processes.

Over recent decades, there have been numerous studies demonstrating the ability to measure sea ice surface properties such as roughness using various remote sensing techniques and instruments and on different scales (Beckers et al., 2015; Gupta et al., 2014; Landy et al., 2015; Von Saldern et al., 2005). Techniques and instruments that are widely

used to observe and monitor changes in the sea ice cover and dynamics include lidar (e.g., ATM, ICESat-2); multi-angular optical (e.g., MISR); radar altimetry (e.g., CryoSat2), synthetic aperture radar (e.g., Sentinel-1); passive microwave (e.g., SSM/I, AMSR-E); sonar (e.g., submarine), and more recently, Interferometric Synthetic Aperture Radar (InSAR, e.g.; Radarsat-2, Sentinel-1).

It is thus important to identify the spatial and temporal scales of key sea ice processes and characteristics and then identify a remote sensing approach that can adequately resolve the processes. Table 1 lists some important processes and characteristics of sea ice. Except for sea ice edge and ice extent, sea ice roughness can be used to characterize sea-ice processes mentioned in this table.

Table 1. Remote sensing of some important processes and characteristics of sea ice.

Sea ice process or characteristic	Spatial scale of the process	The temporal scale of the process	Remote sensing technique
Ice-type, ice age (e.g., first year vs. multi-year ice)	km	Months to years	Visible/IR, Radar/Laser Altimeter, and Passive Microwave, Synthetic Aperture Radar (SAR), Scatterometer

Snow cover on sea ice	km	Weeks to months	Passive Microwave and Scatterometer
Melt pond detection	10s to 100s of m	Weeks to months	Visible/IR
Sea ice albedo	km	Weeks to months	Visible/IR
Ice motion, convergence (hummocks, compression ridges), and divergence (leads)	10s of m	Weeks to months	Passive Microwave, Scatterometer, SAR
Ice edge	km	Months to years	Visible/IR, Passive Microwave
Ice extent	km	Months to years	Visible/IR, Passive Microwave, SAR, Scatterometer

Satellite remote sensing can provide monitoring, analysis, and mapping capabilities for the Arctic environment that can address and resolve mentioned challenges and limitations (Comiso, 1991; Teleti and Luis, 2013).

One advantage of retrieving sea ice parameters such as surface roughness, thickness, concentration, and melt pond from satellite measurements is that it provides larger spatial coverage and enables mapping of surface change and detection between seasons (Landy et al., 2015; Walker et al., 2006). Satellite imagery can provide long-term global observation data with sufficient spatial, spectral, and temporal coverage which makes it a very useful tool for retrieving sea ice parameters (Teleti and Luis, 2013). This has motivated researchers to try to estimate sea ice parameters from satellite imagery because of its large spatial and temporal coverage over the Arctic.

Multi-angular optical remote sensing data have been used to identify and monitor surface texture and roughness. Multi-angle Imaging Spectroradiometer (MISR) is one sensor from that category. MISR imagery collects passive optical multi-angle remote sensing observations where the sensor measures and records the amount of the reflected sunlight at nine different view zenith angles and four spectral bands (Diner et al., 2005). The spectral range that MISR covers is the optical and near-infrared bands. Each camera covers four spectral bands, and it takes 7 minutes to observe each scene from all 9 angles.

One of the main values of MISR data is its simultaneous multiangular reflectance information that creates a link between structural characteristics and radiative quantities of a scene (Diner et al., 1999a). The 9 different viewing cameras on MISR simultaneously

measure the reflection anisotropy of a scene which is influenced by the structural characteristics of the scene such as morphology, geometric orientation, and roughness of reflecting elements. These structural characteristics will influence the radiative characteristics of the scene and will give rise to patterns of angular reflectance in measurements from the scene which are independent of spectral signatures in MISR data. In the context of sea ice surface roughness, interpreting and taking advantage of this multiangle information in measurement data will provide structural clues and information about the sea ice surface and can be used to improve modeling accuracy and to find diagnostic information about sea ice surface (Diner et al., 2005). MISR can complement SAR imagery for operational ice mapping (Nolin et al., 2002). MISR can resolve areas of very thin ice that may be confused with multiyear ice in SAR imagery. Also, in melt season when distinguishing between sea ice and open water in SAR data is difficult, MISR data could provide useful ice-mapping information.

One limitation of MISR is that since it is a passive sensor relying on reflected radiation, it has limited operation in high latitudes during late fall and wintertime. In the Arctic, these periods are dark most of the day and sunlight is not enough to illuminate the target with sufficient radiance. Also, MISR spectral bands cannot penetrate clouds and therefore cannot operate in bad weather conditions.

MISR data has been used in several studies to retrieve and measure surface properties of sea ice over the Arctic (Kharbouche and Muller, 2019; Nolin et al., 2002; Nolin and Mar, 2019; Nolin and Payne, 2007; Stroeve and Nolin, 2002). Nolin et al. (2002) demonstrated that MISR multiangular reflectance data, which represent the angular signature of the sea

ice surface, can be used to characterize sea ice surface roughness (Nolin et al., 2002). They defined a qualitative proxy named Normalized Difference Angular Index (NDAI) by combining imagery data from three MISR cameras. Nolin et al. (2019) demonstrated that angular signatures of sea ice surfaces have the potential to create quantitative maps of sea ice surface roughness. They developed an empirical relationship between multiangular reflectance data from MISR images and sea ice surface roughness measurements from ATM field campaigns over the Arctic. They employed and developed a weighted nearest neighbor algorithm to derive estimates of roughness values for new, unseen MISR data samples. Their study demonstrated that the proposed method can characterize and quantify sea ice physical roughness and has the potential for creating maps of surface roughness over the whole Arctic by using MISR multi-angular reflectance data (Nolin and Mar, 2019). Mosadegh and Nolin (2020) developed a data processing software pipeline for MISR images and created maps of sea ice roughness over the Arctic (Mosadegh and Nolin, 2021, 2022, 2020).

There are several challenges related to gaining knowledge about sea ice characteristics in polar regions: accessibility to those regions is difficult, obtaining enough in situ measurement in the vast arctic environments is hard and not feasible for most locations in that harsh environment, and retrieving sea ice surface roughness from satellite imagery is challenging. Another major challenge in gaining insight into surface properties of sea ice from satellite images in the polar regions is that the Arctic is a cloudy region, which causes MISR images to often contain extensive areas of cloud cover. Detecting and masking clouds, particularly over the polar regions in remote sensing images is a challenging task

because the frozen ground, sea ice, and snow have similar spectral reflectance characteristics to clouds i.e., we try to detect a white object such as a cloud over a white and bright surface such as snow and ice in the Arctic. A sensor like MISR will measure backscattered electromagnetic radiation that is reflected from a scene on the surface of the earth in a similar spectral range and this originates from trying to measure clouds on a highly reflective background such as snow and ice. This results in the problem of detection and mapping of clouds in remote sensing images over snow- and ice-covered surfaces such as the Arctic region.

Furthermore, the size of image data sets from remote sensing platforms is growing and it is impossible to analyze and evaluate a large amount of imagery data manually and visually with human operators. Therefore, cloud detection is considered the first challenging step in preprocessing of data analysis systems that process remote sensing images. This challenge highlights the need for an optimized automated monitoring and classification system for the growing flow of data. On the other hand, recent advances in the development of machine learning algorithms that are optimized for large image datasets together with vast amounts of available remotely sensed data present new opportunities to confront these challenges.

Given the need for efficient algorithms that have high accuracy with high computational efficiency (Diner et al., 1998), the inherent spectral and angular information patterns in the MISR data (Diner et al., 2005), and the advancement of deep learning models as great pattern recognition models and their applications in remote sensing big data sets (Zhu et

al., 2017), we have identified a set of needs to address in this proposed research study. These include:

- Developing an image processing software system with the capability of geolocation of each MISR image to be able to create maps of sea ice roughness over the Arctic by creating a mosaic from each single MISR image.
- Designing and developing machine learning algorithms for MISR data to detect and mask clouds over the Arctic and to discriminate cloudy images and white surface backgrounds by taking advantage of the inherent angular patterns in MISR data to increase the accuracy of cloud detection over the Arctic.

The overarching goal of this research was to develop and implement new and highly efficient data-driven methods for sea ice analysis and to develop the necessary data processing infrastructure to analyze the large volume of imagery data from the Multi-angle Imaging SpectroRadiometer (MISR) sensor. This will lead to a deeper understanding of sea ice roughness, spatial and temporal patterns, providing insights into the impacts of a changing climate. Therefore, this research has 2 main components which are presented in chapters 2 and 3:

Chapter 2 presents the first component of this research which involves developing, implementing, and testing an image processing system and sea ice surface roughness product using a K-nearest neighbor (KNN) algorithm expanding on the earlier work on Nolin and Mar (2019) to encompass the entire Arctic region for two seasons (April and July) and two years. In the initial study, we developed our model by using the KNN

algorithm and with 3 feature inputs. In this research, we have developed a data processing system that produces georeferenced sea ice roughness raster-based images that can be mosaicked to produce Arctic-wide maps of sea ice roughness to produce Arctic-wide maps of sea ice roughness for spring and summer. This processing system and its data products can help the sea ice research community to gain insights into the seasonal and interannual changes in sea ice roughness over the Arctic.

Chapter 3 presents the second component of this research which involves developing a machine-learning binary cloud classifier based on a neural network approach using MISR data to detect and map clouds over sea ice. The Arctic is a cloudy region. MISR images over the Arctic often contain extensive areas of cloud cover but because of similar spectral reflectance characteristics, clouds and sea ice are often difficult to distinguish. Our developed algorithm classifies each pixel in MISR images as cloudy or clear by taking advantage of MISR's nine different viewing angles. The cloud data will become a valuable data set on its own, improving our estimates of cloudiness over this important region.

Chapter 4 presents the conclusion and summarizes our findings.

Chapter 2

A New Data Processing System for Generating Sea Ice Surface Roughness Products from the Multi-angle Imaging SpectroRadiometer (MISR) Imagery

Ehsan Mosadegh ^{1,*}, and Anne W. Nolin ²

¹Atmospheric Sciences Graduate Program

University of Nevada, Reno

Reno, NV 89557, USA

emosadegh@nevada.unr.edu

²Department of Geography

University of Nevada, Reno

Reno, NV 89557, USA

anolin@unr.edu

Correspondence: emosadegh@nevada.unr.edu.

Abstract

Sea ice roughness can serve as a proxy for other sea ice characteristics such as thickness and age. Arctic-wide maps that represent spatial patterns of sea ice roughness can be used to better characterize spatial patterns of ice convergence and divergence processes. Sea ice surface roughness can also control and quantify turbulent exchange between sea ice surface and atmosphere and therefore influence surface energy balance at the basin scale. We have developed a data processing system that produces georeferenced sea ice roughness raster-based images that can be mosaicked to produce Arctic-wide maps of sea ice roughness. This approach starts with top-of-atmosphere radiance data from the Multi-angle Imaging SpectroRadiometer (MISR). We used red-band angular data from three MISR cameras (Ca, Cf, An). We created a training data set in which MISR pixels were matched with co-located and concurrent lidar-derived roughness measurements from the Airborne Topographic Mapper (ATM). We used a K-nearest neighbor algorithm with the training data to calibrate the multi-angle data to values of surface roughness and then applied the algorithm to Arctic-wide MISR data for two 16-day periods in April (spring) and July (summer). After georeferencing the roughness images, we then mosaicked each 16-day roughness dataset to produce Arctic-wide maps of sea ice roughness for spring and summer. Assessment of the datasets shows good agreement with independent ATM roughness data not used in model development. A preliminary exploration of spatial and seasonal changes in sea ice roughness for two locations shows the ability to characterize the roughness of different ice types and the results align with previous studies. This processing system and its data

products can help the sea ice research community to gain insights into the seasonal and interannual changes in sea ice roughness over the Arctic.

Keywords: sea ice; surface roughness; remote sensing; MISR

1. Introduction

The Arctic is warming faster than any region on the planet (Rantanen et al., 2022). Sea ice is highly sensitive to this rapid climate change (Holland et al., 2006; Kumar et al., 2020; Meier et al., 2014; Mueller et al., 2018; Notz and Community, 2020; Stroeve and Notz, 2015), and it has been rapidly declining over the past three decades in the Arctic region (Kwok and Rothrock, 2009; Meier et al., 2007; Stroeve and Notz, 2018). Since 1962, spaceborne sensors have mapped sea ice characteristics and have served as a valuable resource for understanding changes in the Arctic cryosphere (Cavalieri et al., 1999; Comiso, 2002; Comiso et al., 2008; Parkinson et al., 1999; Serreze et al., 2003). In situ and airborne data, acquisitions are challenging in the polar regions due to difficulties in accessing such a vast and extreme environment. Thus, satellite remote sensing has become a valuable technique for performing Arctic-wide spatiotemporal analysis, especially mapping sea ice characteristics. Satellite remote sensing techniques have been used in numerous studies to retrieve and map properties of sea ice over the Arctic (Farrell et al., 2020; Kharbouche and Muller, 2019; Kwok et al., 2009; Landy et al., 2015; Yi et al., 2005). These techniques provide the Arctic research community with sea ice characteristics such as ice age, extent, albedo, thickness, motion, and roughness. Sea ice surface roughness influences synthetic aperture radar and scatterometer retrievals of sea ice type (Segal et al.,

2020), but few studies have explicitly and quantitatively mapped the roughness of sea ice on an Arctic-wide basis (Farrell et al., 2020; Landy et al., 2015).

Dynamics and thermodynamic processes impact and modulate properties of sea ice such as ice thickness, ice age, ice extent, melt pond extent, and surface roughness. These properties consequently influence the surface energy balance and planetary boundary layer processes such as turbulent fluxes of momentum (drag) and sensible/latent heat over the ice surface (Andreas et al., 2010; Arya, 1973; Petty et al., 2017; Steiner et al., 1999). Sea ice surface roughness establishes the linkage with atmospheric processes through boundary layer turbulence (Arya, 1973, 1975; Petty et al., 2017). Sea ice surface roughness topography has spatial and temporal variations and this will reflect in spatial and temporal patterns of other sea ice parameters such as aerodynamic roughness length and drag coefficients (Castellani et al., 2014; Petty et al., 2017). These parameters are needed to estimate wind stress and boundary layer processes in climate and atmospheric numerical models (Guest and Davidson, 1991; Lüpkes et al., 2013, 2012; Steiner et al., 1999). Sea ice surface roughness affects how surface meltwater spread across the surface. Melt ponds on smooth ice can aggregate and spread across a larger area, which consequently, decreases sea ice surface albedo. (Landy et al., 2015; Lei et al., 2016; Lindsay and Zhang, 2005; Moritz et al., 2002; Perovich and Polashenski, 2012; Stroeve et al., 2012; Zhang et al., 2000).

Surface roughness is the variation in surface topography. In this work, the roughness of the sea ice surface is defined as the root mean squared deviations of measured surface elevations from a flat reference surface (Nolin and Mar, 2019). Sea ice surface roughness

is a key property that, although not produced as a standard remote sensing data product, has been mapped and quantified using data from the Multi-angle Imaging SpectroRadiometer (MISR) (Nolin et al., 2002; Nolin and Mar, 2019). One of the main advantages of MISR data is its simultaneous multiangular reflectance information that creates a link between structural characteristics (e.g., surface roughness) and radiative quantities of a scene (Diner et al., 1999a). These structural characteristics will give rise to angular reflectance patterns that are independent of spectral reflectance patterns. For instance, when mapping surface roughness, it is the angular signature that provides information, rather than the more widely used spectral signature (Nolin, 2004; Nolin et al., 2002). Nolin et al. (2002) demonstrated that MISR multiangular reflectance data can be used to characterize sea ice surface roughness. They defined a qualitative proxy named Normalized Difference Angular Index (NDAI) by combining imagery data from three MISR cameras. Nolin and Mar (2019) demonstrated that sea ice angular signatures can be calibrated using airborne lidar-derived measurements of surface roughness and has the potential to create quantitative maps of sea ice surface roughness. They developed an empirical relationship between multiangular reflectance data from MISR images and sea ice surface roughness measurements from the Airborne Topographic Mapper (ATM) field campaigns over the Arctic. They employed and developed a weighted nearest-neighbor algorithm to derive estimates of roughness values for newly acquired MISR data samples. Their study demonstrated that the proposed method can characterize and quantify sea ice's physical roughness and has the potential for creating maps of surface roughness over the whole Arctic by using MISR multiangular reflectance data.

The overarching goal of this research is to develop and implement a new and efficient data processing system that can be used to create roughness maps of sea ice over the entire Arctic. To achieve this goal, we have developed a detailed methodology that i) converts large amounts of MISR multiangular information into sea ice roughness images, and ii) employs a new algorithm that converts the roughness images into geolocated and mosaicked maps of surface roughness over the entire Arctic.

This work supplies the necessary data processing system to analyze the large volume of MISR image data and will lead to a deeper understanding of sea ice roughness over the Arctic.

2. Methods

Our approach builds on the previous work of Nolin and Mar (2019) using a combination of multiangular reflectance data and airborne lidar data to build, calibrate, and validate a surface roughness data model. What is innovative about this work is that we have created a data processing system that will allow the user to process massive amounts of image data to create seamless, Arctic-wide mosaics of sea ice surface roughness.

For this research, we used a subset of MISR images for two 16-day periods to extend and assess the performance and application of the sea ice roughness modeling approach and the processing system. Our study area is the Arctic region, north of 60°N latitude. The time frame covers 16 days in April (spring) and 16 days in July (summer) 2016. April corresponds to the approximate annual peak of sea ice extent and July is approximately the time of melt onset (Landy et al., 2015). We wanted to explore the capacity of our method

for capturing the seasonal changes in sea ice roughness between spring and summer. The periods are 16 days because that is the exact orbital repeat time for MISR, over which the instrument images nearly the entire globe (Diner et al., 1998).

2.1. Description of Data Sets

2.1.1. Airborne Topographic Mapper

The Airborne Topographic Mapper (ATM) is a conically-scanning airborne lidar that measures the surface topography of a swath of terrain directly beneath the path of the aircraft (Studinger, 2014). The ATM instrument has been flown onboard the NASA P-3 and DC8 aircraft as part of NASA's IceBridge campaigns (Studinger, 2014). The instrument flies at a nominal altitude of 500–750 m and uses a scanner angle of 22° with a laser footprint of around 1 m, horizontal accuracy of 0.74 m, and vertical precision of 3 cm. Elevation accuracy determined by Brunt et al. (2017) was found to be typically better than 7 cm.

We used the ATM ICESSEN sea ice roughness data product available from the National Snow and Ice Data Center (NSIDC) in Boulder, CO, U.S., incorporating the surface roughness attribute of sea ice which is different from aerodynamic roughness length. Surface roughness is defined as the root mean square (RMS) of deviation of measured surface elevations from a fitted plane with a specific extent (Studinger, 2014). In this data product, the extent is an 80 m “platelet” from an ATM lidar instrument. Post-processing converts the lidar elevations to surface roughness data. Here, we used ATM ICESSEN-processed data that were resampled from the initial high-volume elevation data set by

fitting overlapping "platelets" of about 80 m in diameter along the flight line using along-track and cross-track slopes. The average and root mean square (RMS) deviation of all elevation points within each platelet are computed to yield values for average elevation and roughness, respectively. We only used the roughness values from the ATM's nadir (zero degrees) scan angle. In the Arctic, ATM-derived sea ice roughness data were collected over the years 2009 – 2019 typically for the months of March, April, and May. Arctic ATM overflights have covered a wide range of sea ice types, including first-year and multi-year ice types.

2.1.2. Multi-angle Imaging SpectroRadiometer (MISR)

MISR is an instrument on the Terra satellite launched by NASA on 18 December 1999. It has nine cameras and each of these cameras views the Earth at a different angle and in four spectral bands. Each camera measures the radiances that are reflected from the Earth's surface to space in a specified direction. MISR uses a Space-Oblique Mercator (SOM) projection/gridding scheme that follows the orbital path of the instrument and preserves the geometry of the multiangular data. There are 233 geographically distinct MISR orbital paths that provide near-global coverage. The 233 paths repeat every 16 days. Each path is subdivided into 180 blocks, with the block numbers increasing from the north to the south pole. Our study area is covered by MISR blocks 1–46. MISR has four spectral bands (blue, green, red, and near-infrared) at each of its nine cameras. The nadir camera has all four bands at a spatial resolution of 275 m while for the non-nadir cameras, only the red band is at 275 m resolution; the other bands are spatially aggregated to 1.1 km resolution (Diner et al., 1999a). Because roughness can be characterized with multiangular data and since we

wish to map roughness at 275-m spatial resolution, we used only the red bands. We used the MISR ML1B2-Ellipsoid data product in this research which includes top-of-atmosphere (TOA) radiance measurements. MISR data were obtained from the NASA Langley Research Center Atmospheric Science Data Center (ASDC) in Hampton, VA, U.S. As with Nolin and Mar (2019), we only used red band radiance information from three MISR cameras (An, Ca, Cf). At high latitudes, the orbits have more spatial overlap. Thus, MISR observes much of the Arctic every two days. Within each image, data from all nine angles are acquired within a seven-minute window.

2.2. Data Preparation and Processing Steps

We began with downloading concurrent and co-located ATM and MISR data. ATM ICESSESSN roughness data (Studinger, 2014) were downloaded from the National Snow and Ice Data Center. MISR Level 1B2 top-of-atmosphere (TOA) radiance data (ML1B2E) were downloaded from the Langley Atmospheric Science Research Center. As previously mentioned, the ML1B2E data are in Space Oblique Mercator Projection (SOM) and each 16-day orbital repeat period has 233 paths; each path is composed of 180 blocks. Blocks are spatially offset to accommodate the curvature of each path. We note that standard HDF-EOS processing routines do not assemble the blocks into smoothly contiguous images. In the next step, we converted TOA radiance to TOA reflectance. Reflectance characterizes the roughness of a surface independent of the magnitude of solar illumination. Each MISR HDF file includes all the blocks in a single MISR path which nominally include 180 blocks. Therefore, we then extracted the number of blocks that cover our study area (blocks 1–46). We then applied a land mask to each block of the MISR data to exclude land areas.

For developing and calibrating our training data set we used sea ice roughness data from ATM measurements. Based on the location information and time of each ATM sample we identified MISR pixels that were co-located and concurrent with each ATM measurement. We then assigned each MISR pixel a roughness value based on the average ATM roughness values within the pixel. We subset the training data set using only those MISR pixels that had 10 or more ATM measurements. After applying this criterion, the final training data set included approximately 11,000 samples for April and 2,200 samples for July. The ATM roughness values allocated to each MISR pixel are the label information for our training data set.

In the prediction step, we used an independent test dataset to predict sea ice surface roughness. These data were not used in building our data model. We developed and tested three models namely simple linear regression (SLR), polynomial linear regression (PLR), and K-nearest neighbor (KNN). For each month (April and July 2016), statistical metrics such as Root Mean Square Error (RMSE), Mean Absolute Error (MAE), Mean Bias Error (MBE), and Coefficient of Determination (R^2) were computed for model assessment. Also, statistical visual tests such as frequency histograms and Q-Q plots were used to evaluate error distributions for each month. Based on these metrics, we selected the KNN algorithm, similar to that used by Nolin and Mar (2019). The original model ran on a single CPU core and was not optimized for big data sets and high-performance computing (HPC) clusters. Processing each input to the data model takes approximately 20 seconds to process a single MISR block on a Linux machine with Intel(R) Xeon(R) CPU E5-2683 v4 processors. Thus, serial processing would take an excessively long time to produce output roughness files. In

this data system, we parallelized the main processing algorithm for HPC clusters. The new algorithm can now run on multiple CPU cores. The input files consist of three land-masked TOA reflectance data files about 8 MB each. Each output file contains the estimated sea ice roughness data and is in a generic raw binary file format with a “.dat” file extension. One output data file covers a single MISR Path/Block combination (e.g., roughness_toa_refl_P233_O087029_B024.dat) with 512 by 1024 pixels and is approximately 24 MB in size.

Georeferenced image data are crucial for creating daily sea ice roughness mosaics. To create a georeferenced, map-projected, multi-band raster from the raw data, we need to have the geo-transformation information for each image. Geo-transformation is an affine transformation with 6 parameters that creates a relationship between the image coordinate space and the georeferenced coordinate space. However, we do not have geo-transformation information for each block which is a challenge for producing a georeferenced raster image from an array of roughness data. On the other hand, MISR L1B2 data files are supplied in one single large HDF file which includes all blocks in a single MISR path, and the only georeferenced information in that file is the location of the top left corner of the first block. Therefore, the first and crucial step for mosaicking the roughness data is to create a georeferenced GeoTIFF image from each roughness file.

We developed an algorithm to transform a roughness array into a raster image and added location information to each pixel in the raster. This algorithm calculates the geographic coordinates of a pixel in the output roughness file from its image coordinates using MISRToolkit (MTK) library functions. Then, we used the ground control point (GCP)

method to embed the geographic information of each roughness pixel to a multi-band georeferenced GeoTIFF raster. We formed GCPs by selecting 85 pixels from each MISR block. This method matches each pixel in the MISR image frame with its corresponding geographical location in a coordinate frame. We used the MTK and Geospatial Data Abstraction Library (GDAL) Python libraries to develop this algorithm. MTK is a program library that has been developed by JPL for processing MISR datasets. It is a simplified programming interface to access MISR L1B2, L2, conventional, and ancillary data products. GDAL is a software library for reading and writing raster and vector geospatial data formats. In all the mentioned processing steps, we used the MTK C and Python libraries and the GDAL Python library to process MISR data files. To create a mosaic from a large data set of produced georeferenced images, we built our mosaicking algorithm by using the GDAL python library and then created maps of sea ice roughness for the whole Arctic. For producing each map, we processed and merged approximately 9000 roughness files. When multiple pixels overlapped, the mosaicking algorithm computed and stored their average in the mosaic. The general steps we described in the data processing section are visualized in Figure 1.

To evaluate the performance of our method, we compared an independent test data set of ATM data samples with their co-located MISR-estimated sea ice roughness values. This subset of ATM data was not used in the building step of our model and was kept aside for model evaluation. We selected this subset from both April and July 2016 data sets, and we calculated statistics from this comparison. Finally, we inspected two arbitrary locations and

visually compared our MISR-derived roughness maps with Landsat 8 and Sentinel-1 images to visually evaluate the accuracy of our MISR-derived surface roughness maps.

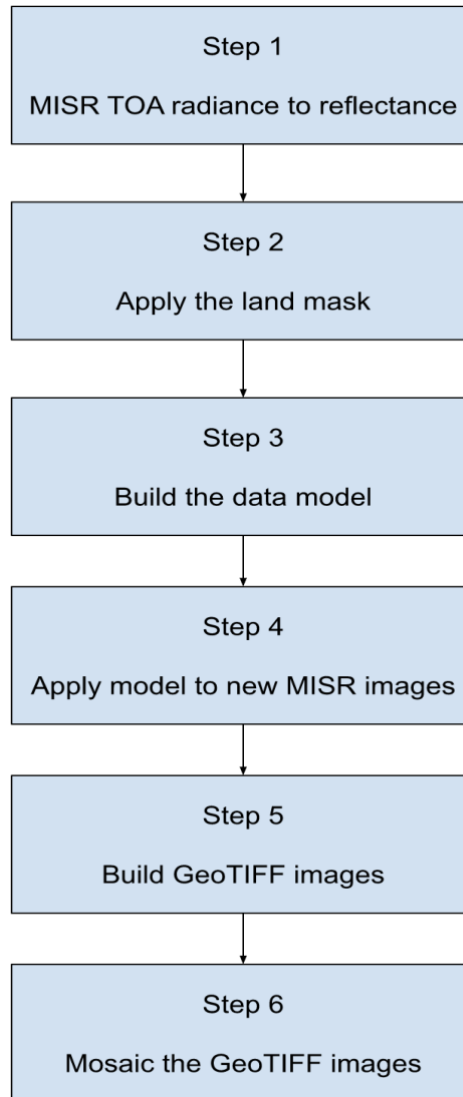


Figure 1. Data processing steps.

3. Results

3.1. Evaluating Model Performance

In the process of labeling MISR images with co-located ATM measurements of sea ice roughness and building the training dataset for our model, we found out that the available number of co-located ATM samples per each MISR image pixel is an important factor in the accuracy of the model predictions. After testing several thresholds for the number of ATM samples per pixel, we concluded that the threshold of at least 10 ATM samples per MISR pixel better represents the surface roughness of sea ice in each MISR image pixel for building our model for this study. Also, we restricted the selection of MISR images to the same day that ATM data were acquired. Therefore, in the process of selecting and subsetting MISR images, we only considered MISR images that were acquired on the same day that ATM measurements were also obtained. We finally developed our model data set based on at least a 10-ATM-samples-per-MISR-pixel threshold on the same day of MISR-ATM overpass over a region and then used our developed model to estimate sea ice roughness for both April and July 2016 to estimate the condition of sea ice roughness for the spring and summer seasons, respectively.

We compared the performance of our KNN model with two other standard parametric regression models: the simple linear regression (SLR) model and the polynomial linear regression (PLR) model. To evaluate the performance of the KNN model with these other regression models, we calculated and compared several statistical measures including R^2 , RMSE, MAE, MBE, and NSE as our performance metrics among all 3 candidate models.

Table 1 presents the performance metrics for both the training and the independent test dataset for the 16 days in April and July 2016. The performance of the developed model is usually evaluated based on its skill on the independent test dataset because this dataset is not used in training the model and therefore this score may be more representative of the true skill of the trained model. A comparison of performance metrics for the independent test dataset in Table 2 illustrates that KNN is the best model for both April and July. For instance, KNN has the highest R^2 for both April and July among all three models. Also, RMSE and MAE bias metrics for April and July on the independent test dataset have lower values compared to two other models for each month. MBE shows the bias of a model and a negative value shows that a model underestimates the modeled roughness. MBE of our modeling results indicates that all three models underestimate roughness. KNN for July has the lowest bias (-0.09 cm) and the highest bias (-0.16 cm) for April, but both bias values are negligible. Because the results of the NSE test metric were similar to R^2 , we did not include the NSE metric results in this table.

Table 2. Statistics of sea ice roughness model performance.

	R^2		RMSE (cm)		MAE (cm)		MBE (cm)	
	training	test	training	test	training	test	training	test
SimpleLinearRegr								
April	0.12	0.13	6.49	6.44	4.99	4.93	0	-0.12
July	0.06	0.05	5	4.9	3.7	3.6	0	-0.14

PolyLinearRegr	R²		RMSE (cm)		MAE (cm)		MBE (cm)	
	training	test	training	test	training	test	training	test
April	0.28	0.29	5.87	5.8	4.45	4.36	0	-0.15
July	0.11	0.09	4.77	4.84	3.56	3.6	0	-0.09

KNN	R²		RMSE (cm)		MAE (cm)		MBE (cm)	
	training	test	training	test	training	test	training	test
April	0.66	0.5	4.05	4.91	2.81	3.39	-0.08	-0.16
July	0.58	0.32	3.29	4.2	2.21	2.82	-0.04	-0.09

The frequency distributions of ATM observations and MISR-estimated sea ice roughness for independent test datasets for April and July are compared in Figure 2. A visual comparison of the histograms shows that April is rougher than July in our dataset and our method can effectively characterize this difference between the two seasons. These data cover a much greater spatial extent than the previous work by Nolin and Mar (2019), and R^2 is comparable to this previous work. Eventually, based on these performance metrics we selected KNN as our prediction model for our dataset.

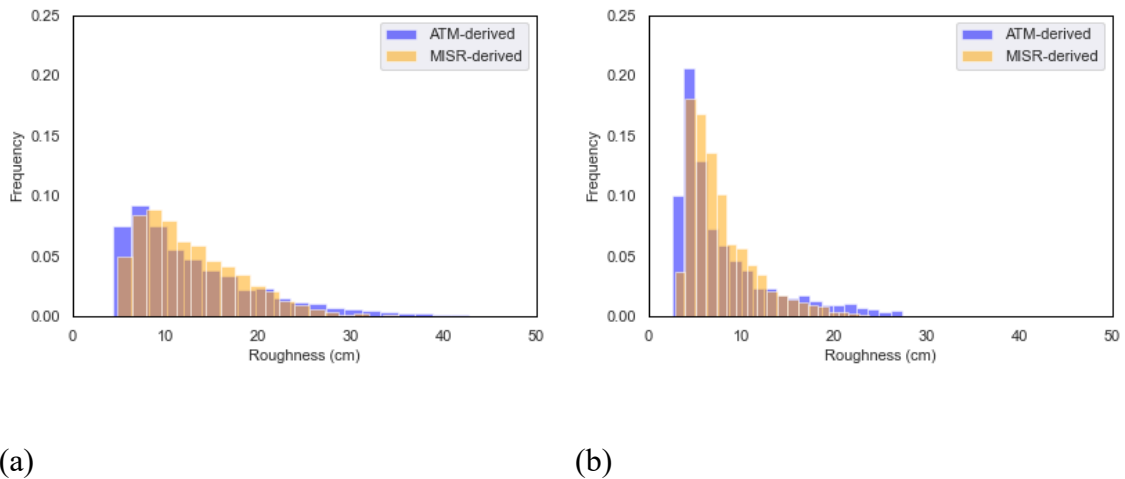


Figure 2. Histograms comparing MISR-estimated (using the KNN model) and ATM-observed (independent test data) sea ice roughness for (a) April and (b) July 2016. The brown color is where the blue and orange colors overlay each other.

To describe and compare the error distributions we generated quantile-quantile plots (Q-Q plots) and histograms for each month. The Q-Q plot is a scatter plot with the quantiles of the sample data (error values in our plots) on the vertical axis and the expected normal value on the horizontal axis. Q-Q visual test assumes normality and tests if residuals follow a normal distribution. If the points fall approximately along the 45-degree reference line, the two data sets come from a population with the same distribution, i.e., indicating that MISR-derived roughness values must be normally distributed. Figure 3 shows the Q-Q plots that visualize roughness errors in two datasets for each month.

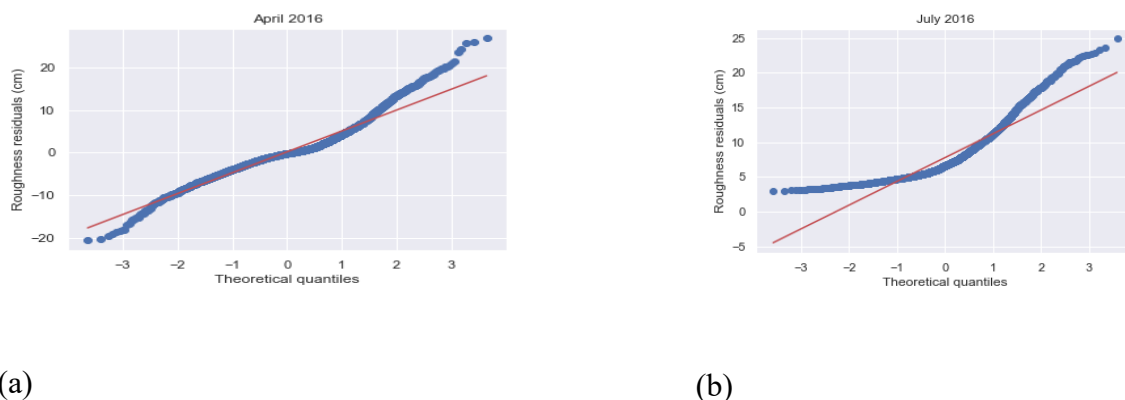
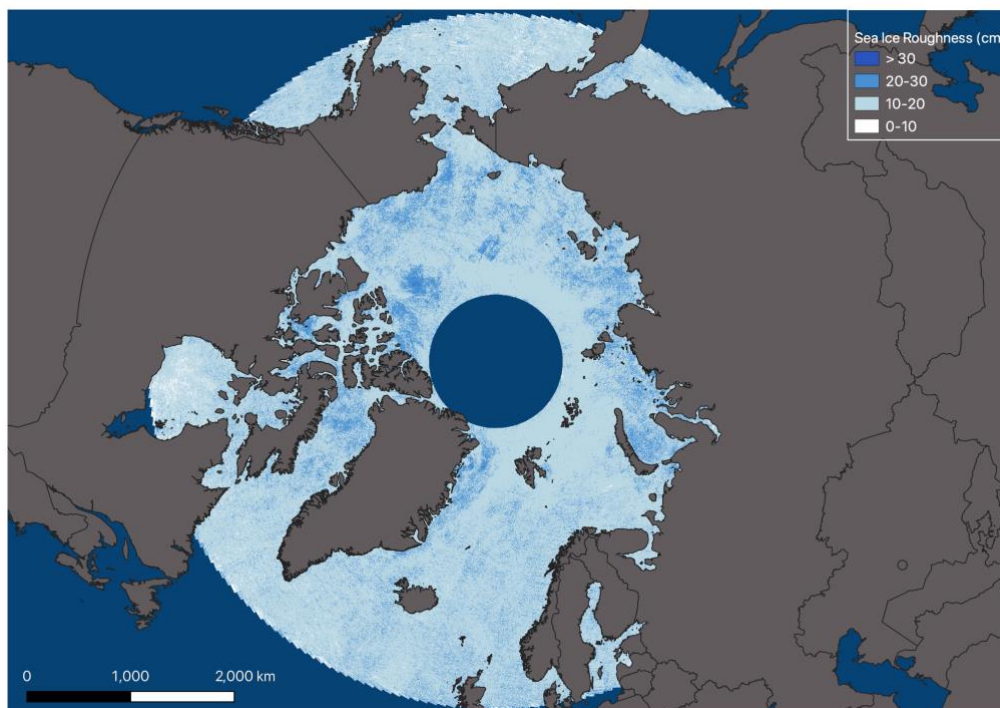


Figure 3. Q-Q plots for the April and July 2016 datasets (a and b) show the error distribution of MISR-estimated roughness for (a) April and (b) July 2016.

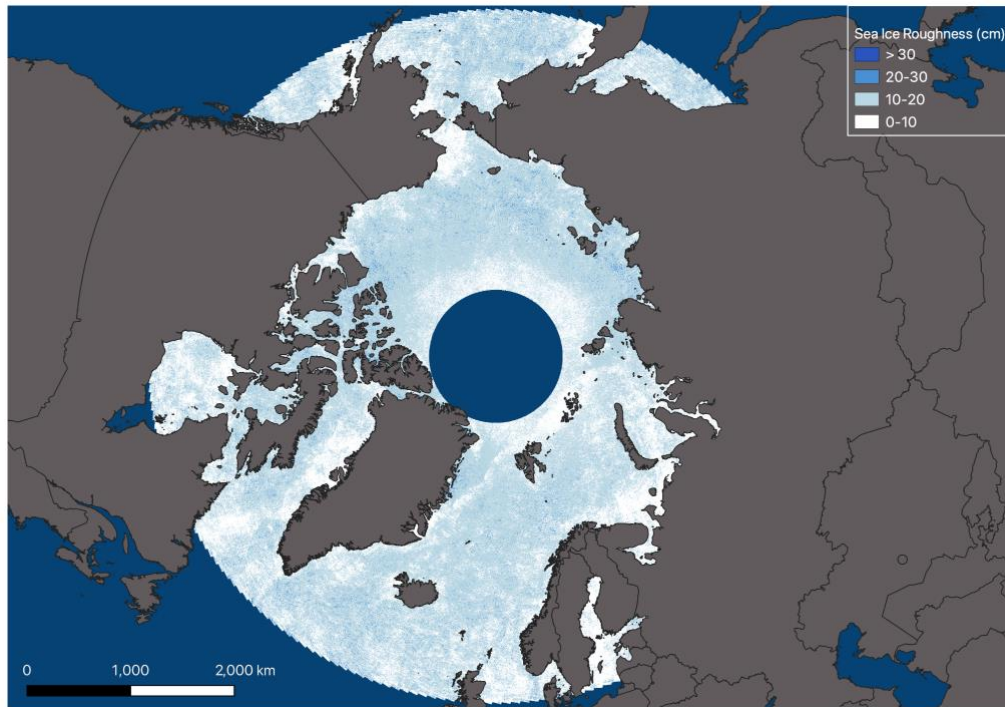
Both Q-Q plots show deviation from the straight line, suggesting that sample residual quantiles are quite different from the theoretical quantiles and are not normally distributed. Also, both plots are skewed at their tails, but the July residual distribution is more skewed at both tails compared to the April distribution. The Q-Q plots for April (Figure 3a) show that residual points fall along the best-fit line in the middle of the graph, but the differences increase on both ends of the distribution of residuals. This indicates that residuals have more extreme values at both ends of the residual distribution. The Q-Q plots for July (Figure 3b) show a considerable deviation from the straight line on both ends of the distribution, indicating that the residuals are not normally distributed. The histograms in Figure 2 confirm that the distribution is not bell-shaped but skewed.

3.2. Spatial Patterns of Arctic Sea Ice Roughness

After evaluating the performance of the method in the previous section, we produced maps of sea ice roughness over the Arctic which included regions where ATM measurements were not available. Figure 4 shows the produced maps of sea ice roughness for April (spring) and July (summer) 2016 over the Arctic. These maps were created with the method described in Section 2. Each map is produced by georeferencing every single MISR image and then creating a mosaic from all image blocks starting from block 1 to block 46 acquired in 16 days from MISR daily paths over the study area. MISR orbits repeat themselves every 16 days. Each map was created from about 9000 MISR image blocks. Overlapping blocks were averaged to create a mosaicked Arctic-wide map of mean sea ice roughness for each season. For the task of georeferencing and building the mosaic of images, we used the GDAL library.



(a) April



(b) July

Figure 4. Spatial patterns of mean sea ice surface roughness derived from MISR images (275 m resolution) over the Arctic region for 16-day periods of (a) 15–30 April 2016 and (b) 10–25 July 2016.

Maps in Figure 4 visualize the spatial patterns in sea ice roughness over the Arctic. They also show the temporal differences and the development of sea ice roughness averaged over the study area for the spring and summer of 2016. In the spring map, we can see that

there are some rough regions where the MISR-estimated roughness values exceed 30 cm. The Arctic Ocean north of the Canadian Arctic Archipelago, and the Fram Strait east of Greenland are some notably rough regions in the spring map that are depicted as dark blue. Figure 5 shows these two regions in spring and summer. For instance, there is a very rough area of sea ice in the Arctic Ocean north of the Canadian Arctic Archipelago in the spring map (Figure 5a and Figure 5b). That region usually is covered with multi-year ice fields (Kwok, 2015; Kwok et al., 2020). The roughness of multi-year ice is somewhat smoothed by melt from the previous summer. Thus, this multi-year ice is maybe less rough than blocky and deformed first-year ice where ridges and deformations have not yet experienced melt.

Another rough region on the spring map is the Fram Strait (Figure 5c and Figure 5d). This region is characterized by convergence and divergence features of sea ice and is an important gateway to exporting multiyear sea ice (Kwok et al., 1998) and is one of the most dynamic regions in the Arctic Ocean, especially in spring (Min et al., 2019). Dynamic modifications of the ice motion to the ice thickness such as ridging in that region may contribute to the thickness of sea ice and roughness patterns in that region. This suggests that the patterns of roughness in the spring map in that region could be attributed to the export of thick multiyear sea ice. Furthermore, Figure 5 shows the seasonal change of sea ice roughness from spring to summer and the decrease in sea ice roughness values in those regions. In the spring map, sea ice roughness values at the Arctic Ocean (Figure 5a) and Fram Strait (Figure 5c) are high, while the summer map shows that sea ice at the Arctic Ocean (Figure 5b) and Fram Strait (Figure 5d) have much lower roughness values. This

seasonal change in sea ice roughness could be associated with the melt processes of the sea ice during the warm season (Kwok et al., 2009; Landy et al., 2015). Summer melting reduces the thickness of the sea ice cover and contributes to the reduction of the surface roughness of sea ice.

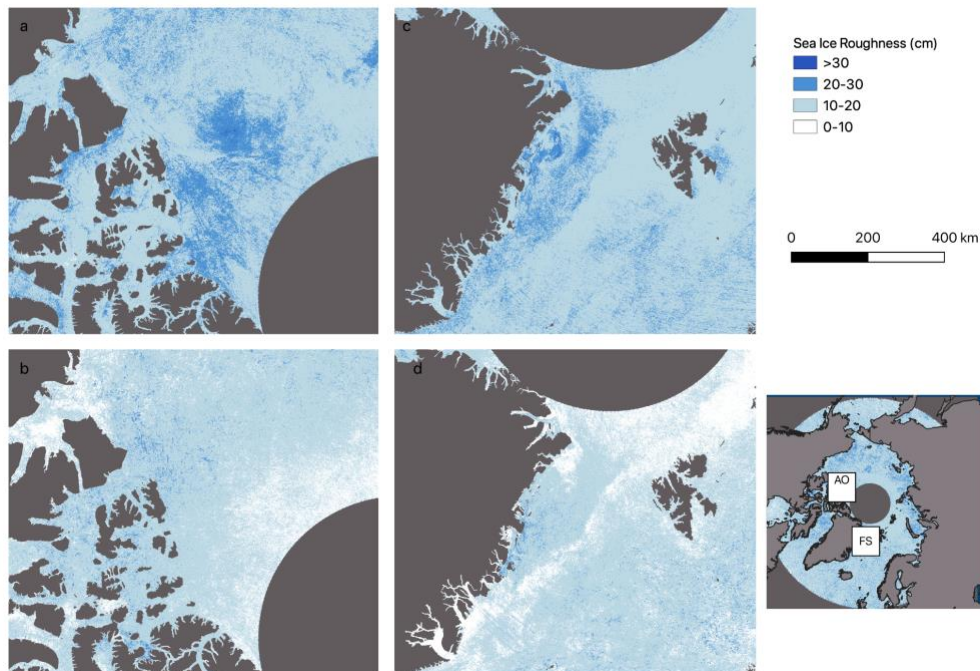
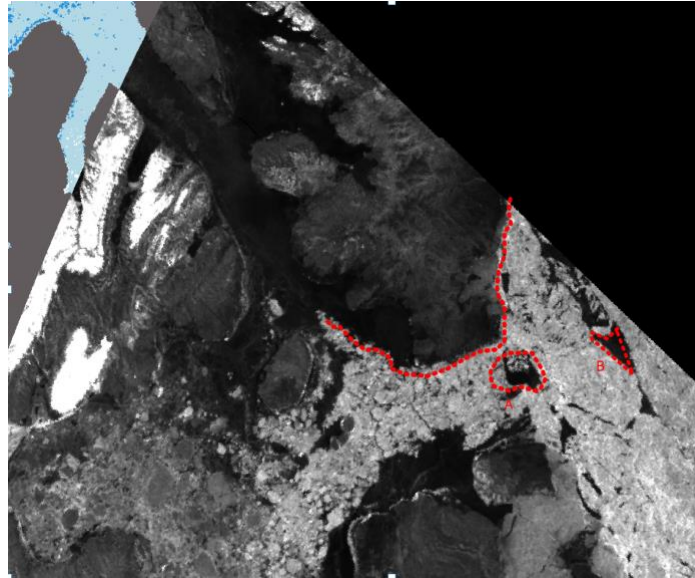


Figure 5. Mean MISR-derived sea ice surface roughness for two locations: the Arctic Ocean (AO) north of the Canadian Archipelago, and Fram Strait (FS) east of Greenland. (a) the AO in spring, (b) the AO in summer, (c) FS in spring, and (d) FS in summer.

To evaluate the accuracy of our MISR-derived surface roughness maps and compare it with other remote sensing methods, we inspected two arbitrary locations and compared our MISR-derived roughness maps with Landsat 8 and Sentinel-1 images for each arbitrary region of interest. **Error! Reference source not found.** shows an arbitrary location in the

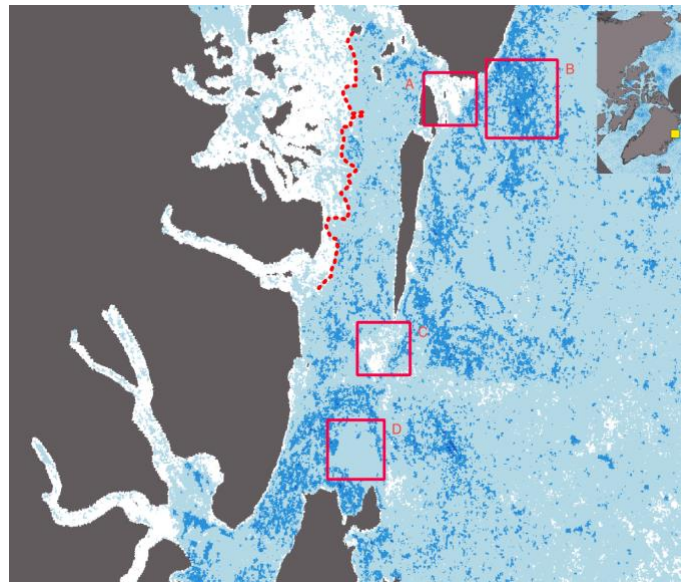
Canadian Archipelago in April 2016. **Error! Reference source not found.**^a is our MISR-derived roughness map for an arbitrary location north of the Canadian Archipelago. **Error! Reference source not found.**^b and **Error! Reference source not found.**^c show the same region from Landsat 8 and Sentinel-1 views, respectively. We selected and inspected zones A and B to investigate if our maps can characterize areas of land-fast ice in that region. For example, zones A and B in our roughness maps represent a smooth area. Landsat 8 image shows that zones A and B might be land-fast ice and open water. Sentinel-1 also shows zones A and B in dark color which represents a smooth surface which could be open water or land-fast ice. Also, by visually inspecting our roughness map, we drew a dashed line to separate smooth and rough surfaces of ice. One side of the dashed line is smooth ice which is represented as dark in the Sentinel-1 image and the other side that looks bright represents a rough surface. There is an obvious transition from a smooth to a rough surface pattern in Landsat 8 and Sentinel-1 images and our roughness map shows the same surface pattern.

We also inspected some areas adjacent to the east coast of Greenland in our July roughness map. **Error! Reference source not found.** shows an arbitrary location at the Fram Strait in July 2016.

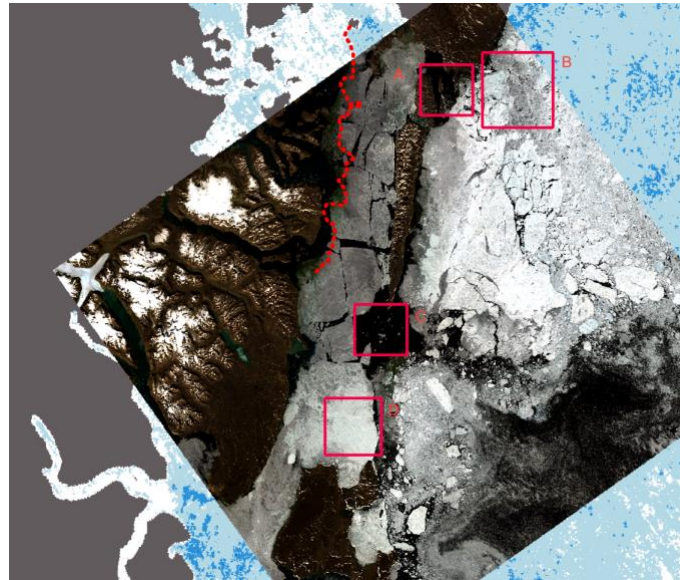


(c)

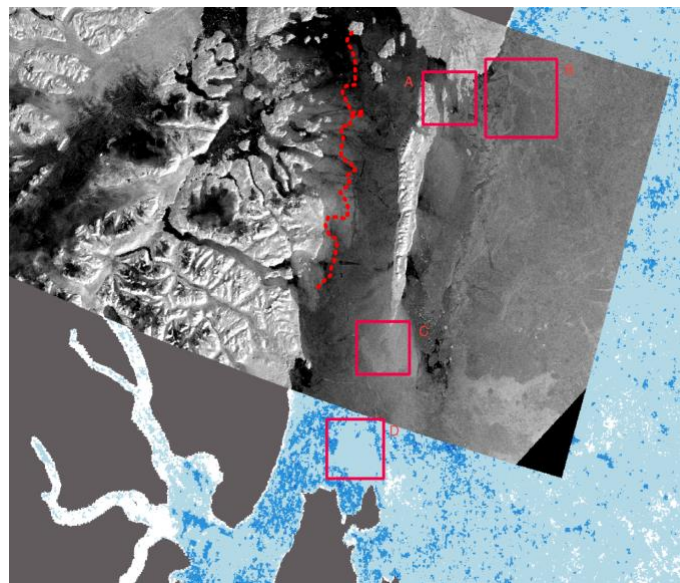
Figure 6. Comparison of (a) MISR-derived roughness map with (b) Landsat 8 and (c) Sentinel-1 images at an arbitrary location north of the Canadian Archipelago on 29 April 2016 at 116.1 W and 77.5 N.



(a)



(b)



(c)

Figure 7. Comparison of (a) MISR-derived roughness map with (b) Landsat 8 for July 20th and (c) Sentinel-1 for July 19th images at an arbitrary location at the Fram Strait in July 2016 at 18.7 W and 76.5 N.

Like **Error! Reference source not found.**, we inspected a few zones in our MISR-derived roughness map for July 2016 at Fram Strait and compared them with Landsat 8 and

Sentinel-1 images for the same location. The Sentinel-1 image was not available for the same location on July 20th, so we used a Sentinel-1 image for July 19th instead. In **Error! Reference source not found.** we can see in the Landsat 8 image that zones A and C are open water. We can see the same pattern in our roughness map and zones A and C are mapped in white and represent a smooth surface. Although the Sentinel-1 image was taken a day before the Landsat 8 image, it represents the same surface patterns. Zone D in the Landsat 8 image represents a smooth surface, and our roughness map has also captured that surface pattern and mapped it as a smooth surface. Also, the Landsat 8 image shows that zone B is a mixture of smooth and rough zones. Our roughness map shows the same pattern and maps zone B in light and dark blue color which represents a mixture of smooth and rough surface patterns. The same pattern can be observed in zone B in the Sentinel-1 image.

Also, we visually inspected the Landsat 8 image and drew a dashed line and separated smooth ice and open water from rough ice. We can see in the Landsat 8 image that one side of the dashed line is open water which is represented as dark in the image and the other side includes sea ice which is represented as bright in the Landsat 8 image. In our roughness map, we can see this surface pattern clearly on both sides of the line and this transition from smooth to rough surface patterns is mapped with a transition from white to blue-colored areas. Landsat 8 and Sentinel-1 images and our roughness map show the same surface pattern. Therefore, we can conclude that our roughness maps can characterize surface patterns of smooth and rough ice.

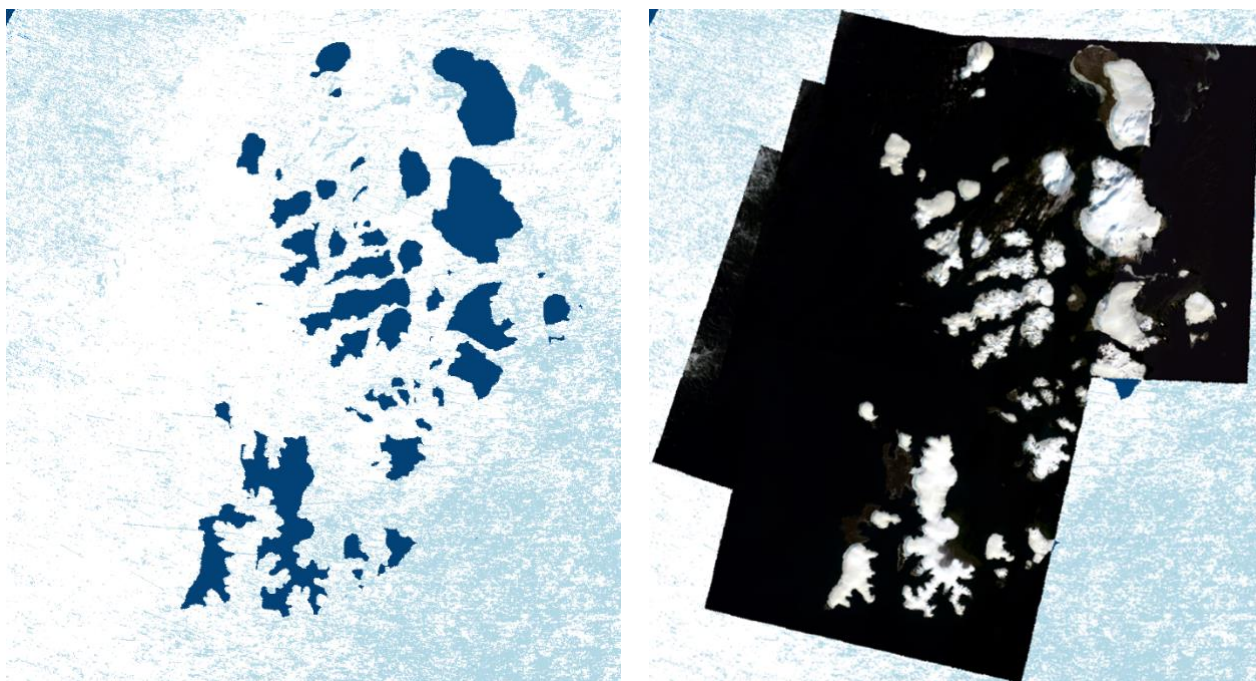
4. Discussion

Several potential sources of error and uncertainty should be taken into consideration for future improvements of this method. These include cloud detection, the number of ATM samples in a MISR pixel and their temporal co-occurrences in the training data, and challenges in distinguishing between open water and very thin smooth sea ice. Among all mentioned error sources, clouds and cloudy training data sets are likely to contribute to a significant part of the error. If clouds were present in images that were used to build the training data set, this would introduce noise to the training data set. The goal of this research was to present the capabilities of this data product and since cloud masks over sea ice tend to classify sea ice as clouds we did not use a cloud mask in this research, and we left this option to the preference of the users of this data processing system. We anticipate improved cloud detection and masking capabilities in future analyses. Cloud-free MISR images were manually selected that were concurrent and co-located with the ATM data. Also, since ATM flights occurred during clear sky days, using MISR images during the same flight day of ATM implicitly suggests that that day was not cloudy. However, finding cloud-free images for a specific location in the Arctic to study seasonal changes remains a significant challenge.

The number of ATM samples in each MISR pixel that were used to estimate that pixel's roughness is important for the accuracy of the MISR-derived roughness. MISR pixels that have only a few ATM roughness observations were found to have a low agreement in terms between modeled roughness and ATM-measured roughness. We found that having a minimum of 10 ATM values in a MISR pixel improved the accuracy of model output when

labeling MISR pixels with ATM information. We also found that the model output was improved when the MISR images used to build the training data set were selected from the same day as the ATM flight. This differed from the methodology described by Nolin and Mar (2019), who used data from ± 1 day of the ATM overflight.

At present, our model is not able to distinguish between very smooth, thin first-year sea ice (e.g., “grease ice” or “dark nilas (Sea Ice Glossary) and what may be open water. We considered incorporating a reflectance threshold that could detect dark open water, but very thin first-year ice can be both smooth and dark. Thus, the July sea ice roughness maps are likely to include open water as well as sea ice. For instance, a subjective visual examination of a Landsat 8 reflectance image shows that pixels mapped as 0–10 cm surface roughness appear to be ice-free. Figure 8 shows the ice-free area around the Zemlya George archipelago for a cloud-free period from 10–15 July 2016. The MISR-derived roughness map for the period 10–25 July 2016 shows this same area as having a roughness of 0–10 cm.



(a)

(b)

Figure 8. Comparison of (a) MISR-derived roughness map with (b) Landsat 8 for the ice-free area around the Zemlya George archipelago for a cloud-free period from 10–15 July 2016. Dark-blue patches in our MISR-derived map are the Zemlya George island.

The histogram in Figure 2b which compares July ATM and MISR-derived sea ice roughness, shows that our model underestimates the frequency of sea ice roughness values less than about 5 cm. While the difference in spatial resolution between MISR and the ATM roughness product (275 m vs. 80 m) is likely responsible for the undercount of smooth ice, it may also be the case that some parts of the MISR pixel are smooth ice and other parts are open water.

5. Conclusion

In this paper, we described how we developed our sea ice roughness data product. We also provided estimations of the surface roughness of sea ice by creating Arctic-wide maps of sea ice roughness for spring and summer seasons from MISR multiangular reflectance information. We showed that this appears to be a promising method for quantifying and mapping Arctic-wide sea ice surface roughness and can characterize spatial patterns and variability of sea ice surface topography and seasonal changes in sea ice roughness over an extensive area for different seasons at a horizontal scale of 275 m. The spatial patterns and their seasonal changes are consistent with other similar studies mentioned in the results section. To the best of our knowledge, this is the first attempt at creating Arctic-wide maps of sea ice roughness from MISR multiangular information.

There are strengths and limitations to any remote sensing technique. MISR data has several advantages such as a long record of data (2000–present), near-global coverage, and spatial resolution down to 250 m. Especially the broad angular coverage which is independent of its spectral coverage makes it a unique source of information. However, building data models from MISR multiangular information reveals some of its limitations that must be taken into consideration such as it requires lidar data for calibration, and if the study region is over the Arctic, images tend to be cloudy and dark. To understand the full benefit, this data product still requires additional interpretation by sea ice researchers. Also, this data product can be a helpful complement to other remote sensing techniques such as ICESat-2, SAR, and high-resolution optical data. Given the quality of the MISR imagery, MISR-estimated roughness is best used for understanding the spatial patterns of sea ice roughness

as well as the detailed daily estimates of sea ice roughness. Also, averaged Arctic-wide maps are more useful for understanding and diagnosing the changing patterns of mean sea ice roughness in seasonal and long-term studies of sea ice roughness in the Arctic. Therefore, considering that sea ice roughness can serve as a proxy for other sea ice characteristics such as thickness and age, this data product can be beneficial to improving our understanding of the roughness patterns over the Arctic region and can be a helpful tool for the Arctic science community.

Author Contributions: Conceptualization, A.W.N. and E.M.; methodology, E.M., and A.W.N.; software, E.M.; validation, E.M.; formal analysis, E.M.; investigation, E.M.; resources, A.W.N.; data curation, E.M.; writing—original draft preparation, E.M.; writing—review and editing, A.W.N.; visualization, E.M.; supervision, A.W.N.; project administration, A.W.N.; funding acquisition, A.W.N. All authors have read and agreed to the published version of the manuscript.

Funding: This research was funded on a subcontract (#1623719) through the MISR Project, NASA/Jet Propulsion Laboratory.

Institutional Review Board Statement: Not applicable.

Informed Consent Statement: Not applicable.

Data Availability Statement: The code and data presented in this study are openly available via the Zenodo repository at <https://doi.org/10.5281/zenodo.7155214>.

Acknowledgments: These data were obtained from the NASA Langley Research Center Atmospheric Science Data Center.

Conflicts of Interest: The authors declare no conflict of interest.

Chapter 3

Development and Evaluation of a Neural Network-based Cloud Detection Algorithm for Multi-Angle Imaging SpectroRadiometer (MISR) Imagery

Ehsan Mosadegh ^{1,*}, and Anne W. Nolin ²

¹Atmospheric Sciences Graduate Program,

University of Nevada, Reno

Reno, NV 89557, USA

emosadegh@nevada.unr.edu

²Department of Geography

University of Nevada, Reno

Reno, NV 89557, USA

anolin@unr.edu

Correspondence: emosadegh@nevada.unr.edu.

Abstract

The Arctic is a cloudy region that often causes MISR images to contain extensive areas of cloud cover. We developed a binary cloud detection algorithm based on a neural network approach for identifying cloudy and clear pixels in Multi-angle Imaging SpectroRadiometer (MISR) images. The training dataset was constructed by using top-of-atmosphere red band values from nine different cameras for two different months, April and July, covering various regions in the Arctic. The labels in the dataset were first visually assessed and divided into training and test datasets with a 70/30 split, with 70% of the dataset used for training and 30% used for independent test data. The resolution of the MISR red band is 275 m, resulting in a spatial resolution of 275 m for the developed classifier.

The performance of the developed model was assessed using confusion matrices and performance statistics such as Precision, Recall, F score, and Accuracy. The results indicate that the developed neural network-based binary classification algorithm showed good performance in classifying pixels into cloudy and clear categories in MISR images. The algorithm also provides a significant advantage over existing MISR cloud mask products such as SDCM and ASCM in terms of accuracy and spatial resolution, with a resolution of 275 m. The results also suggest that the performance of the classifier varied between the two seasons, with better performance for clear pixels in April 2016 and better performance for cloudy pixels in July 2016. These results can be used to develop and improve more accurate classification algorithms by indicating areas for improvement in future iterations

of the algorithm. The developed labeled dataset can also be used for further studies in the field of remote sensing and image processing.

1. Introduction

The Arctic is a cloudy region that often causes MISR images to contain extensive areas of cloud cover. Detecting and masking clouds, particularly over the polar regions in remote sensing images is a challenging task and cloud masks perform poorly over snow-covered terrain due to the potential similarity between multispectral signatures of snow and cloud pixels in certain situations (Stillinger et al., 2019). Clouds and cloudy images are likely to contribute to the significant part of error and uncertainty in satellite remote sensing image analysis. Using cloudy images to build training datasets contributes to uncertainty in model outcomes. Therefore, the task of cloud detection and masking is considered an important preprocessing step for most data analysis systems that process remote sensing images, and having an accurate cloud classifier can reduce the uncertainty in model predictions. Furthermore, the size of image datasets from remote sensing platforms is growing (Lynnes and Huang, 2022) and it is impossible to analyze and evaluate a large amount of imagery data manually and visually with human operators. Therefore, there is a need for optimized automated monitoring and classification systems for the growing flow of remote sensing data.

The MISR instrument is capable of collecting reflectance information of a scene at multiple angles. This creates the reflectance angular signature from a scene that is independent of the spectral information of that scene (Diner et al., 1999a). This quality in MISR data

together with its long-term data collection and global coverage makes this data source a unique resource for remote sensing applications in a variety of fields, including climate science, meteorology, ecology, and land use planning. MISR cloud mask products provide valuable information for a variety of applications in remote sensing such as climate and weather modeling, air quality monitoring, understanding cloud dynamics and properties, and improved accuracy of remote sensing products such as land cover mapping (Diner et al., 2005). Using cloud masks can help improve the accuracy of these products by removing clouds from the observed signals.

MISR has three cloud mask standard data products, which have been developed by the MISR science team specifically for use with MISR images (Diner et al., 1999b, 1999c). The three cloud masks are designed to classify each MISR pixel individually as either cloudy or clear, with high confidence or low confidence at 1.1 km resolution. The Radiometric Camera-by-camera Cloud Mask (RCCM) (Diner et al., 1999c) calculates the cloud mask for each of the nine MISR cameras by calculating and setting three thresholds that differentiate and classify each pixel into four categories combining cloudy and not cloudy with high and low confidence. The thresholds are derived using an automated procedure and are a function of sun angle, view angle, relative sun-view azimuth angle, time, and place on the globe. The Stereoscopically-Derived Cloud Mask (SDCM) (Diner et al., 1999b) uses a feature image matching technique and stereo observations from multiple MISR cameras to determine whether a pixel is cloudy or clear. The Angular Signature Cloud Mask (ASCM) (Diner et al., 1999c) is based on the Band-Differenced Angular Signature (BDAS) technique and uses blue and near-IR bands. It uses a

thresholding technique based on calculating the differences between the angular signatures of the two most oblique cameras, Cf and Df, and then classifies a pixel into four categories combining cloudy and clear with high and low confidence. Thresholds for the BDAS depend on the view zenith angle, solar zenith angle, view azimuth angle, surface type, and season. Each of these cloud masks works very well under certain conditions. However, each method has its limitations and no single one appears to be robust enough for detecting clouds, particularly over bright surfaces such as snow and ice in the Arctic. For instance, in the case of detecting clouds over polar regions, RCCM fails to detect clouds effectively over areas with sea ice, and SDCM shows sea ice and water as ‘No Retrieval’ in some cases (Genkova et al., 2005). Therefore, Genkova et al (2005) recommend that the most appropriate combination of masks to use over snow and ice surface types is a combination of SDCM and ASCM.

An algorithm that combines the strength of all three cloud mask products, i.e. RCCM, SDCM, and ASCM was also explored to create a single consensus cloud mask product for MISR (Genkova et al., 2005). However, the suggested algorithm struggles to classify regions with snow and ice cover accurately. The algorithm still uses SDCM and ASCM for regions with snow and ice cover and classifies regions into cloudy and clear categories at the spatial resolution of 1.1 km.

Statistical classifiers are developed and used on MISR images using linear correlation matching, quadratic discriminative analysis, and Gaussian kernel support vector machine methods (Shi et al., 2008, 2007, 2004). Physical features were developed from remotely sensed data and then used to classify MISR image pixels into “cloudy” and “clear” sky

classes. The region of permanent sea ice in the Arctic Ocean, snow-covered and snow-free coastal mountains in Greenland, and permanent glacial snow and ice were selected to build physical features that contain sufficient information to separate clouds from ice- and snow-covered surfaces. These studies showed promising results in achieving high classification accuracy for polar clouds. However, they only used data from a single path of MISR, which limits the generalization of the results.

The Support Vector Machine (SVM) approach has been used to classify cloudy pixels from MISR. A supervised classifier using the SVM technique was also developed and used by combining spectral, angular, and texture features to classify each pixel of MISR images into different classes (Mazzoni et al., 2007). This method reached approximately 81% accuracy of cloud classification globally at an 1100-meter pixel level with an 8% misclassification error for cloudy pixels as sea ice. This method showed the potential for improving classification accuracy by incorporating additional information and developing a classifier that can fit better into MISR data. SVM was also used to train a classifier to analyze clouds on a global scale and classify MISR image pixels (Garay et al., 2005). This method used large feature vectors containing many raw features from different camera angles and spectral bands throughout a large spatial neighborhood. The results suggest that this method can be very effective for many global image pixel classification problems. However, this method was confined to latitudes less than 60° in both hemispheres.

Neural network algorithms have also been used to develop and build cloud mask classifiers for polar regions for different sensors. These methods do not rely on traditional threshold-based methods. This method was applied to classify MODIS pixels using several developed

parameters from extensive radiative transfer simulations (Chen et al., 2018) and results showed that its performance is significantly better than the MODIS Cloud Mask (MOD35 C6) during winter seasons over snow-covered areas in the mid-latitudes. Also, this algorithm showed great performance when applied to SLSTR images to build a binary cloud classifier (Poulsen et al., 2020). The algorithm was applied to polar regions and used input features such as spectral channels (nine channels), latitude, longitude, satellite zenith angle, solar zenith angle, and surface-type flags. A similar technique was used to train a binary cloud classifier for the Visible Infrared Imaging Radiometer Suite (VIIRS) images (White et al., 2021). The model inputs were several channels expressed either as a reflectance or brightness temperature, together with a binary land–water mask, solar zenith angle, sun glint zenith angle, and the absolute value of latitude. The trained model was applied to the Greenland region and outperformed the Continuity MODIS-VIIRS Cloud Mask (MVCM) and the NOAA Enterprise Cloud Mask (ECM) in most conditions.

Other studies have investigated methods such as mixing spectral information with ancillary data for MODIS imagery (Riggs and Hall, n.d.), band-differenced angular signature (BDAS) technique for MISR imagery (Di Girolamo and Davies, 1994; Di Girolamo and Wilson, 2003), rule-based and threshold setting for Sentinel-2 imagery (Zekoll et al., 2021), deep convolutional neural network (CNN) for Landsat 8 imagery (Hughes and Kennedy, 2019), and spectral, and spatial signature threshold tests for AVHRR (Stowe et al., 1999).

As mentioned earlier, methods such as statistical classifiers, stereo-based algorithms, and thresholding techniques have been shown to have limitations such as poor functionality over snow and ice surfaces, extra calculation steps, and the use of ancillary information.

Moreover, the existing MISR cloud classifiers were not able to take full advantage of MISR's multiangle capabilities. Additionally, cloud masks are only available at 1.1 km spatial resolution. To address these limitations, we developed a binary cloud classifier for MISR images that can detect and mask clouds at a resolution of 275-m, which matches the resolution of our sea ice roughness model (Mosadegh and Nolin, 2022). Our method has fewer input parameters and only uses reflectance data from 9 cameras with no ancillary information or thresholding techniques, making it more flexible and generalizable on new images. We built only 2 classes in our algorithm, which can have advantages such as more generalizability/applicability to other regions for detecting only cloudy pixels, but also disadvantages in that only 2 general classes can be detected as a binary classifier.

Consequently, this study intends to develop a neural network-based binary cloud detection and classification algorithm for MISR images that can provide cloud mask products with a particular focus on the Arctic region. The remainder of the manuscript is organized as follows. Section 2 describes the satellite data and the development of the neural network-based method. The performance of the algorithms is evaluated in Section 3, and Section 4 discusses the results followed by Section 5, which summarizes our key findings and makes recommendations for future work.

2. Methodology

The overall approach in developing the cloud detection algorithm was to utilize the angular patterns of reflectance of clouds to differentiate cloudy pixels from clear pixels over sea ice. The algorithm was developed using a machine learning approach trained on cloudy-

and clear-sky pixels over two regions in the Arctic for two time periods. The following describes the steps we took to develop the cloud detection algorithm.

The Multi-Angle Imaging SpectroRadiometer (MISR) is an instrument on board the Terra satellite, which was launched by NASA on 18 December 1999. MISR image data are available from February 2000 to the present. The MISR instrument has nine pushbroom cameras. Each of its nine cameras samples radiances that are reflected from the Earth's surface to space in four spectral bands (blue, green, red, and near-infrared) from nine different directions. There are 233 geographically distinct MISR orbital paths that provide near-global coverage. The 233 paths repeat every 16 days. Each path is subdivided into 180 blocks, with the block numbers increasing from the north to the south pole. Our study area is covered by MISR blocks 1–46. The nadir-viewing camera has all four spectral bands and a spatial resolution of 275 m, while for the non-nadir cameras, only the red band is at 275 m resolution; the other bands are spatially aggregated to 1.1 km resolution. Since we wish to distinguish clouds from sea ice based on angular reflectance properties and do so at a spatial resolution that matches our MISR sea ice roughness product, we aim to classify pixels at 275 m spatial resolution and thus use only the red bands. We used the MISR ML1B2-Ellipsoid data product (Diner, 2013) in this research which includes top-of-atmosphere (TOA) radiance measurements. MISR data products in Hierarchical Data Format (HDF) were obtained from the NASA Langley Research Center Atmospheric Science Data Center (ASDC) in Hampton, VA, U.S. We subset the data product to include only the red band radiance information for the nine MISR cameras (Da, Ca, Ba, Aa, An, Af, Bf, Cf, Df). At high latitudes, the orbits have some spatial overlap. Thus, MISR

observes much of the Arctic every two days. Within each image, data from all nine angles are acquired within a seven-minute window.

For this research, we used a subset of MISR images for two 16-day periods to build and label a training dataset and eventually build our cloud binary classifier. Our study area is the Arctic region, north of 60°N latitude. The time frame for selecting sample data covers 16 days (15-30) in April (spring) and 16 days (10-25) in July (summer) 2016. These periods correspond to periods as in Mosadegh and Nolin (2022). We wanted to develop a training dataset and a cloud binary pixel classifier for our sea ice roughness model and to test the capacity of our developed classifier for detecting and masking cloudy pixels in our sea ice roughness dataset between spring and summer. The periods are 16 days because that is the exact orbital repeat time for MISR, over which the instrument images nearly the entire globe.

To build and label our training and test dataset for our cloud binary classifier, we used our labeling algorithm to label each MISR pixel. We developed and used this algorithm in our previous research (Mosadegh and Nolin, 2022) to label MISR reflectance images with Airborne Topographic Mapper (ATM) airborne lidar data. To build the training dataset this algorithm finds the associated reflectance values from all 9 cameras for a specific MISR pixel and then finds the co-located cloud mask value for that pixel as the label of the pixel. Each pixel sample in the dataset has the necessary information such as path, orbit, block, line, and sample numbers to reference that pixel in post-processing steps. The algorithm locates and extracts TOA reflectance values that come from each of the 9 cameras and allocates them to each specific pixel in the training dataset. This method enabled us to

collect and build the angular signature from each pixel from 9 cameras. It also finds and extracts the cloud mask values for each pixel from MISR cloud mask products such as SDCM and ASCM.

Labeling the training dataset for this research entailed two main steps: First, we used cloud classification information from MISR, SDCM, and ASCM cloud masks to label sampled pixels in our training dataset first. We selected these two cloud masks based on Genkova et al (2005) which recommends that the most appropriate combination of masks to use over snow and ice surface types is a combination of SDCM and ASCM. We only selected high-confidence (HC) and low-confidence (LC) labels from SDCM and ASCM products to label our training dataset. Then, in the next step, we assessed every single image pixel in our training dataset visually to confirm pixel labels are correct. For instance, if a pixel label from consensus products was 44 it meant the two products detected that pixel as clear HC. If a pixel label from SDCM and ASCM was 11 it meant the two cloud masks detected that pixel as cloudy HC. Also, if a pixel label from SDCM and ASCM was 41 it meant the SDCM classified that pixel as clear HC (4), but ASCM classified that pixel as cloudy HC (1). When we were visually assessing each pixel in our training dataset, we checked and confirmed if a pixel was actually clear or cloudy with HC or not. Then, two experts performed the subjective cloudy/clear identification on the labeled dataset from the previous step. We reclassified each pixel in our training dataset based on our visual assessment and voting and updated and corrected our training dataset. We performed this step to build our training datasets for both April and July 2016. We used only red band TOA reflectance values from all nine cameras to build our training dataset for each month, April

and July. After updating the training datasets with labels from our visual assessment step, we developed our training dataset for April and July 2016. Our visually assessed labels worked as the true value and the basis for comparison for our future accuracy assessment.

Using our labeling algorithm, we built our training dataset with TOA reflectance values from nine different cameras. We decided to build our training dataset with 9 red-band cameras at 275-meter resolution. Therefore, the input feature vector to our classifier is an array of red band TOA reflectance from nine cameras which forms the angular reflectance signature for a specific pixel. We selected sample pixels from different paths that represented several different locations in the Arctic in both April and July.

After collecting sample pixels for both months, we performed quality control as the preprocessing step on the developed training datasets. To control the quality of the training data, we performed the following steps: For any missing values in a sample pixel, we removed that row with missing data from the training dataset. If any data sample contained negative values, the entire data sample was removed from the training dataset. Moreover, we removed the whole data sample for a pixel if it had constant and/or zero values and filtered for pixels that had values from all 9 cameras for a single pixel. The final training dataset for each month had the following columns in the dataset: path number, orbit number, block number, line number, sample number, red-band TOA reflectance values from all 9 cameras at 275 meters, MISR SDCM-ASCM cloud labels, and our visually-assessed and confirmed labels. Then we shuffled and then assigned 70% of the samples to train and 30% to test the algorithm.

We developed, trained, and tested several neural network architectures for binary classification to identify cloudy and clear pixels in MISR images. We tested different hyperparameters such as the number of layers and the number of nodes per layer to find the best architecture for the model for each season. We eventually selected the best architecture in terms of its performance statistics on independent test data. We built the neural network model using the Keras Sequential API. The details of the final architecture of the model are presented in the results section. We finally reported the performance of the classifier on the test dataset. The algorithm and its training datasets were developed using Python programming language and scikit-learn and TensorFlow libraries, which are open-source machine learning libraries for Python.

In our previous study, we found that clouds and cloudy images are likely to contribute to a significant part of the error when developing our sea ice roughness model, i.e., if clouds were present in images that were used to build the training data set for the sea ice roughness model, this would introduce noise to the model results (Mosadegh and Nolin, 2022). To reduce uncertainty and noise in training data developed from MISR images and to detect and mask clouds and cloudy pixels in MISR images, we developed our classifier for 2 classes: cloudy and clear (snow, ice, or open water).

After training the algorithm on our training dataset, we assessed the performance of the classifier on an independent test dataset. The test dataset is the portion of the data that is kept aside as independent data to evaluate and report the performance of the trained model on unseen new data. In our developed binary classifier, we assigned the positive class, e.g., class 1, to the cloudy class, because the cloudy class as the positive class is the class that

is of interest and importance in our study. Therefore, we mapped HC clear pixels (44) to 0, and HC cloudy pixels (11) to 1. We reported the performance of the developed classifier using a confusion matrix and the following set of metrics on independent test datasets for each month, April, and July (Olson and Delen, 2008):

$$\text{Precision} = \frac{TP}{TP+FP} \quad (1)$$

$$\text{Recall} = \frac{TP}{TP+FN} \quad (2)$$

$$\text{Accuracy} = \frac{TP+TN}{TP+TN+FP+FN} \quad (3)$$

$$F = 2 \frac{\text{precision} \times \text{recall}}{\text{precision} + \text{recall}} = \frac{2 TP}{2 TP+FP+FN} \quad (4)$$

These metrics use True Positive (TP), False Positive (FP), True Negative (TN), and False Negative (FN) to calculate performance statistics. Precision describes the precision of the classifier in correctly detecting a class, e.g., the proportion of samples that were predicted to be in class 1 (cloudy) and belonged to class 1. Recall describes the proportion of samples that belong to the cloudy class and that were correctly classified by the model. Accuracy is defined as the number of truly classified sample labels divided by all samples. It describes the proportion of samples that were correctly classified by the model. F-score is a harmonic mean of precision and recall and provides a balance between the two metrics.

3. Results

In this study, we developed a binary classification algorithm for identifying cloudy and clear pixels in MISR images. The training dataset was built using red band values extracted from 9 different cameras for two different months, April and July. As was described in the methods section, we visually checked the labeled pixels and divided the dataset into training and test datasets, with 70% used for training and 30% used for testing. The training dataset consisted of 2712 pixels for April 2016 and 5802 pixels for July 2016, while the test dataset consisted of 678 pixels and 1451 pixels for April and July, respectively. Samples were selected from different MISR paths covering different regions in the Arctic. The resolution of the MISR red band is 275 m, therefore the spatial resolution of our classifier is 275 m.

We trained the neural network algorithm on the training dataset and examined different architectures and hyperparameters to find the model with the best performance for each season. We eventually selected a fully connected neural network with dense layers as our final model. Figure 9 shows the architecture of the developed neural network model. The algorithm has three dense layers with 64, 32, and 2 neurons, respectively. The input layer has nine inputs. The first two hidden layers use the ReLU activation function, while the output layer uses the sigmoid activation function. The model is then compiled with the `binary_crossentropy` loss function, the accuracy metric, and the Adam optimizer with a 0.001 learning rate.

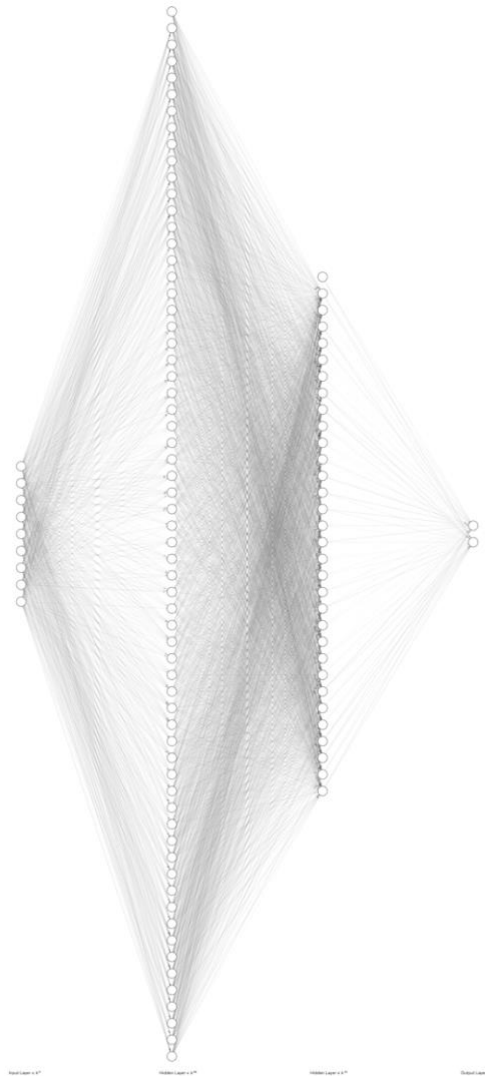


Figure 9. The architecture of the developed neural network model for both seasons. The algorithm has 3 dense layers and 9 nodes at its input layer. From left to right, there are 64, 32, and 2 neurons in each hidden layer. The network has 2 output nodes that represent 2 classes, clear and cloudy.

Overall, our developed labeled dataset contained path, orbit, block, line, sample, and red band values from nine cameras, MISR consensus cloud mask labels, and visually

assessed labels for each pixel. The following section describes the results of the classification tasks on the test dataset for detecting cloudy pixels. Examples have been selected to illustrate the capabilities of the Neural Network-based classifier (NNCM) for different seasons, rather than a comprehensive assessment of their performance.

Table 3. Confusion matrix for April 2016.

	Predicted classes		
Actual classes		Clear	Cloudy
	Clear	531	4
	Cloudy	56	87

Table 4. Confusion matrix for July 2016.

	Predicted classes		
Actual classes		Clear	Cloudy
	Clear	374	102
	Cloudy	37	938

Table 5. Performance statistics for April 2016.

	Precision	Recall	F score
0	0.90	0.99	0.95
1	0.96	0.61	0.74
Accuracy	91%		

Table 6. Performance statistics for July 2016.

	Precision	Recall	F score
0	0.91	0.79	0.84
1	0.90	0.96	0.93
Accuracy	90%		

We evaluated the performance of the algorithm for two different months, April and July 2016, using confusion matrices and performance statistics. The assessment of the performance of the neural network cloud detector was primarily compared against visual assessment.

Tables 3 – 6 show the performance statistics for each season, including Precision, Recall, F score, and Accuracy. We compare the ability of a binary class NN to distinguish between cloudy and clear pixels when given a feature vector containing only TOA reflectance values from the 9 MISR cameras. In a confusion matrix, each row represents a class of true pixels according to expert labels and each column represents the classification decision made by the NN classifier. A perfect classifier, then, would show 100% correct classification down the main diagonal.

The results of the binary classification algorithm for classifying pixels into cloudy and clear in the MISR images are presented in Table 3 and Table 4. Table 3 shows the confusion matrix for April 2016, where the classifier correctly predicted 531 clear pixels and 87 cloudy pixels, while misclassifying 56 cloudy pixels as clear and 4 clear pixels as cloudy. Table 4 shows the confusion matrix for July 2016, where the classifier correctly predicted 374 clear pixels and 938 cloudy pixels, while misclassifying 102 clear pixels as cloudy and 37 cloudy pixels as clear.

In April 2016, the classifier achieved a Precision of 0.90 for clear pixels and 0.96 for cloudy pixels. The Recall was 0.99 for clear pixels and 0.61 for cloudy pixels. The overall accuracy of the classifier was 91%, and the F score was 0.95 for clear pixels and 0.74 for cloudy pixels. These results indicate that the classifier performed well for clear pixels, with high precision and recall, but had a lower performance for cloudy pixels, particularly in terms of recall.

In July 2016, the classifier achieved a Precision of 0.91 for clear pixels and 0.90 for cloudy pixels. The Recall was 0.79 for clear pixels and 0.96 for cloudy pixels. The overall Accuracy of the classifier was 90%, and the F score was 0.84 for clear pixels and 0.93 for cloudy pixels. These results indicate that the classifier performed well for cloudy pixels, with high Precision and Recall, but had a lower performance for clear pixels, particularly in terms of Recall, meaning that it misses identifying some clear pixels in our July dataset.

The model achieved high Accuracy, Precision, and Recall for clear pixels in both months, while the performance for cloudy pixels was lower, with a lower recall observed in April 2016 and a lower Precision observed in July 2016. These results can be used to improve the model and to develop more accurate classification algorithms for cloud detection in remote sensing imagery.

In general, the results suggest that the neural network-based binary classification algorithm showed good performance in classifying pixels into cloudy and clear categories in MISR images. However, the results suggest that the performance of the classifier varied between the two seasons, with better performance for clear pixels in April 2016 and better performance for cloudy pixels in July 2016. These results can be used to develop and improve more accurate classification algorithms by indicating areas for improvement in future iterations of the algorithm.

Here we demonstrate the superiority of our neural network-based cloud detection approach over the traditional threshold-based methods used by MISR (the SDCM and ASCM algorithms). We compared the performance of our binary classification algorithm with the

MISR SDCM-ASCM cloud mask for a selected independent image block and evaluated the accuracy metric for each method. Accuracy was calculated as the ratio of correctly classified samples to the total number of samples.

To illustrate the advantages of our approach, we present an example scene containing clouds here. The image belongs to block 10 from path 149 and orbit 88247 in July 2016. Figure 10 shows a grayscale image of the image block built from the red-band data. Figure 11 shows the false color composite of the image block. We combined the red, green, and blue channels of the CF, AN, and CA cameras to produce this image. Figure 12 shows the same block from the ASCM data product, and Figure 13 presents our NNCM data product for the same block.

We selected 441 pixels from both the NNCM and MISR SDCM-ASCM labels and compared them to our visual assessment, which we took as the true labels of each pixel. We calculated the accuracy metric for this comparison, using only the pixels where both SDCM and ASCM labeled the pixel as either cloudy HC or clear HC. For an unseen block, we randomly selected a few samples for which we had both visually assessed labels and MISR consensus labels available and calculated the accuracy metric for them.

These results show that the NNCM outperforms the MISR consensus cloud mask labels. For the selected image block and sampled pixels, the accuracy of NNCM was 83%, while the accuracy of combined MISR SDCM-ASCM cloud mask products was 1.4%. This indicates a significant improvement in accuracy using our approach compared to the traditional threshold-based methods.

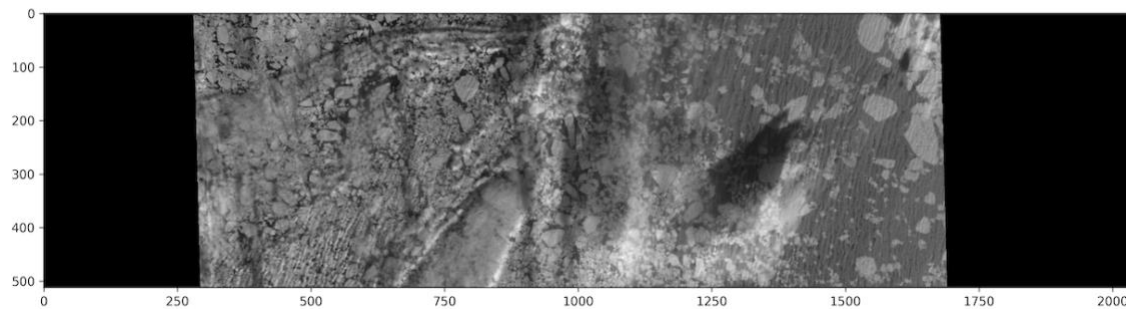


Figure 10. Grayscale image of a cloudy image.

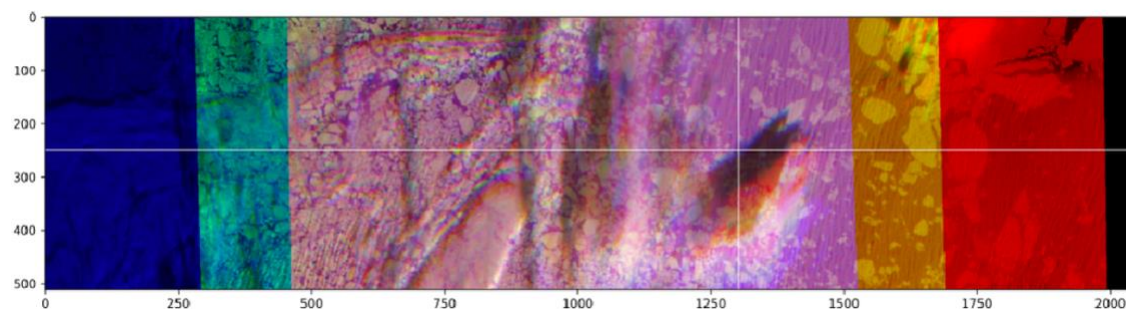


Figure 11. False color composite R(Ca) G(An) B(Cf) image of a cloudy block.

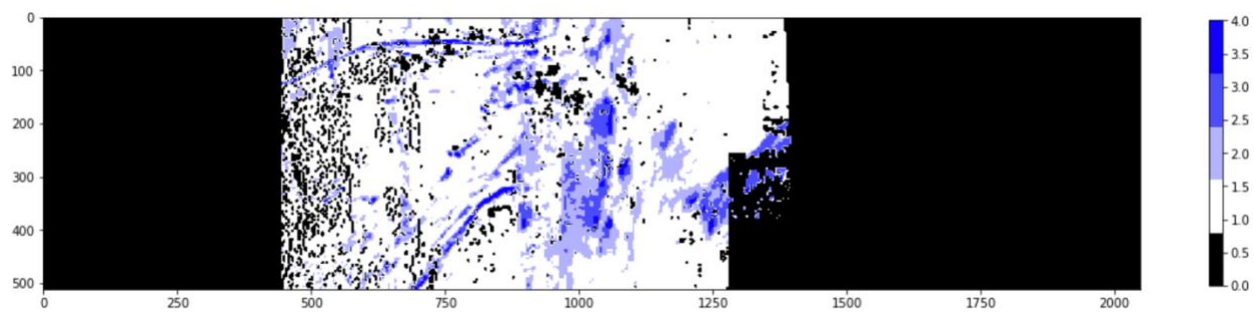


Figure 12. In the ASCM cloud mask, blue is clear HC, and white is cloudy HC.

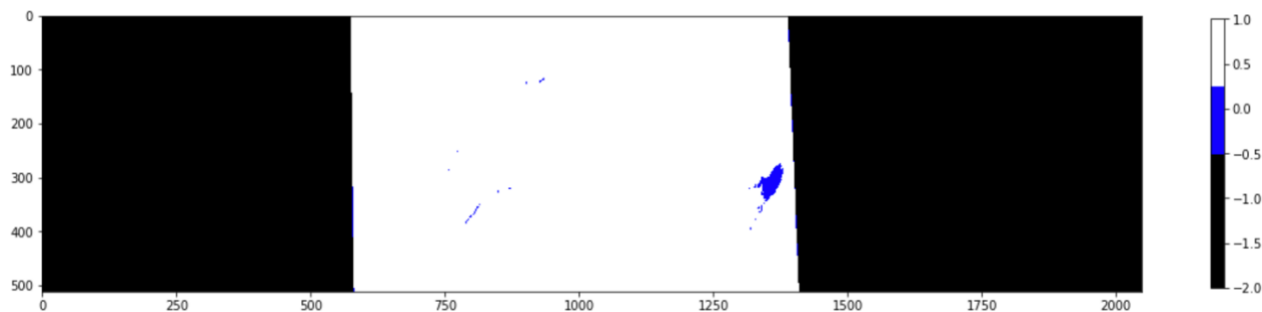


Figure 13. In the NNCM cloud mask, blue is clear, and white is cloudy.

We also calculated the accuracy for SDCM and ASCM labels separately and compared each cloud mask to our visual assessment. For the selected image block and sampled pixels, the accuracy of SDCM was 3.5%, while the accuracy of ASCM was 56%. ASCM had a much better performance compared to SDCM in terms of accuracy based on samples that were taken in this image block. However, compared to ASCM and SDCM, NNCM showed much better performance in terms of accuracy (83%). This indicates that the developed algorithm provides a significant advantage over existing MISR cloud mask products in terms of accuracy and spatial resolution, with a resolution of 275 meters.

4. Discussion and Conclusion

The development of a binary classification algorithm for identifying cloudy and clear pixels in MISR images using a neural network approach is an important step forward in improving the accuracy and speed of cloud detection in remote sensing applications. This is especially important in the Arctic where cloud detection over sea ice has been challenging. In this study, we developed a neural network model and its training dataset

consisting of only red band values extracted from MISR's nine different cameras, for two different months, April and July 2016.

One of the advantages of our neural network-based approach is that the accuracy is not dependent on threshold values. This makes this approach more flexible to generalize to new and unseen data without recalibration or adjustment of the threshold values for each new image. In contrast, geometry-, threshold- and rule-based techniques such as SDCM, RCCM, or ASCM are often limited by the quality of the threshold value chosen, which can lead to incorrect classifications.

Another advantage of this method is that it only uses TOA reflectance values from 9 different viewing cameras as the input to the model. Using this array of inputs makes this method more flexible in handling different types of images, efficient and quicker to process a large amount of data, and potentially easier and better at generalizing to new and unseen data. Furthermore, our developed algorithm provides a significant advantage over existing MISR cloud mask products such as SDCM, ASCM, and RCCM in terms of resolution, with a resolution of 275 meters.

The results of the binary classification algorithm for identifying cloudy and clear pixels in MISR images are promising, but some limitations need to be considered. The developed algorithm was trained on a dataset that was built using only red band values extracted from 9 different cameras for only two different months, April and July 2016, and samples were selected from different MISR paths covering different regions in the Arctic. This could limit the algorithm's generalizability to other months or regions. However, we did choose

samples from different MISR paths covering different regions in the Arctic, which helps to increase the algorithm's applicability. Therefore, it is unclear how the algorithm will perform on data from different regions or during different seasons. However, we also combined both training datasets for April and July and trained a model with that combined training dataset and we noticed the accuracy of the model decreased although not significantly compared to the accuracy for every single dataset.

Additionally, the spatial resolution of the classifier is 275 meters, which may not be sufficient for some applications. Our algorithm provides a significant advantage over existing MISR cloud mask products such as SDCM, ASCM, and RCCM in terms of spatial resolution. Our method only distinguishes between two classes and does not provide cloud detection confidence estimates, which is a limitation compared to SDCM and ASCM which differentiate between more classes (cloud high confidence, cloud low confidence, clear low confidence, and clear high confidence). Additionally, our algorithm struggles to distinguish cloud shadows and thin clouds. This however can sometimes be difficult even for field experts when visually trying to assess and evaluate a scene using RGB composite images.

The confusion matrices for both April and July 2016 show that the classifier was able to correctly classify the majority of clear pixels but had somewhat more difficulty with cloudy pixels. In April 2016, the classifier correctly identified 531 clear pixels and 87 cloudy pixels but misclassified 56 cloudy pixels as clear and 4 clear pixels as cloudy. Similarly, in July 2016, the classifier correctly identified 374 clear pixels and 938 cloudy pixels but misclassified 102 clear pixels as cloudy and 37 cloudy pixels as clear. These

misclassifications could potentially have implications for applications that require more accurate identification of cloud cover.

The Precision, Recall, and F score metrics provide more detailed information about the performance of the classifier. In April 2016, the classifier achieved a Precision score of 0.90 for clear pixels and 0.96 for cloudy pixels, indicating that the classifier was able to accurately classify a high proportion of true positives for both classes. The Recall score was 0.99 for clear pixels but only 0.61 for cloudy pixels, indicating that the classifier had difficulty identifying all of the true positive cloudy pixels. Similarly, in July 2016, the classifier achieved a Precision score of 0.91 for clear pixels and 0.90 for cloudy pixels, indicating good accuracy for both classes. The Recall score was only 0.79 for clear pixels and 0.96 for cloudy pixels, indicating that the classifier had difficulty identifying all of the true positive clear pixels.

There are several sources of error in this study. First, the subjective visual assessment and labeling of cloudy and clear pixels could contribute to errors of omission and commission, both of which would influence the Precision, Recall, and F scores. Having two experts performing the subjective cloudy/clear identification helps but is never foolproof. A second source of error is the algorithm itself, which depends on the nature of the training set. The training data set included a range of cloud types (e.g., cirrus, stratus, multiple cloud layers) over various sea ice types (e.g., fast ice, continuous ice cover, fractured ice cover, ice floes) but we could not include all cloud types over all sea ice types. In terms of relative magnitude, we found that false negatives (FN) and false positives (FP) have a similar

magnitude of the error. To improve our algorithm, we could consider incorporating additional data sources and refining our labeling and visual assessment methods.

In conclusion, the binary cloud classification algorithm developed in this study is highly promising for cloud detection in MISR images over sea ice. This algorithm could be further refined and extended to the Antarctic. It would also be valuable to test this algorithm over the full timeframe of MISR data collection (2000-present) to create a cloud classification product to accompany the sea ice roughness algorithm that was developed by Mosadegh and Nolin (2022).

Results from this study point to the need for additional classes such as thin clouds and cloud shadows. This will require more training data samples and a more robust visual assessment of data. Future research should explore the potential of combining the developed algorithm with other approaches, such as multispectral and multitemporal analyses, to improve the accuracy of cloud detection in MISR images for different categories and classes such as thin clouds and cloud shadows. Moreover, with a global training data set this machine learning approach could be generalized to create a global cloud detection algorithm. The development of accurate cloud detection algorithms is crucial for improving our understanding of the Earth's climate and the impacts of climate change.

Chapter 4

Summary and Conclusions

In this study, we developed and implemented new and highly efficient data-driven methods for sea ice analysis and developed the necessary image processing infrastructure to analyze the large volume of imagery data from the Multi-angle Imaging SpectroRadiometer (MISR) sensor. The system produces georeferenced, high-quality sea ice roughness images by using red-band angular data from three MISR cameras. This data product is used to analyze spatial patterns of sea ice roughness in the Arctic region. We also developed a novel cloud mask algorithm that effectively detects and masks cloudy pixels in MISR images and produces cloud mask data products optimized for our sea ice roughness model. Our methodology utilized various datasets, including MISR images, lidar-derived roughness measurements from the Airborne Topographic Mapper (ATM), and MISR cloud mask data products such as SDCM and ASCM. Overall, this study provides significant insights into sea ice analysis and offers a promising approach to analyzing large-scale data from satellite sensors.

We produced Arctic-wide maps of sea ice roughness from top-of-atmosphere radiance data from MISR images for two 16-day periods in April and July 2016. We did that by building a training data set in which MISR pixels were matched with co-located and concurrent lidar-derived roughness measurements from the ATM data. We calibrated the MISR data to values of surface roughness by using a K-Nearest Neighbor (KNN) algorithm and then applied the algorithm to Arctic-wide MISR data.

We found that the accuracy of the model predictions depends on the number of co-located ATM samples per MISR pixel and concluded that a threshold of at least 10 ATM samples per pixel provides a better representation of the sea ice surface roughness in each MISR image pixel. We restricted the selection of MISR images to those acquired on the same day that ATM measurements were obtained to build the model data set.

We compared the performance of the KNN model with two standard parametric regression models, the simple linear regression (SLR) model, and the polynomial linear regression (PLR) model, and evaluated the models using several statistical measures, including R^2 , RMSE, MAE, MBE. We found that KNN is the best model for both April and July, with the highest R^2 and the lowest RMSE and MAE bias metrics among all three models.

The frequency distributions of ATM observations and MISR-estimated sea ice roughness for independent test datasets for April and July were compared, and we found that this method effectively characterized the difference in roughness between the two seasons in our dataset. We selected KNN as the prediction model for this dataset based on the performance metrics.

This study also examined the spatial patterns of sea ice roughness in the Arctic for the spring and summer of 2016 using data from MISR. The produced maps of sea ice roughness depict the development of sea ice roughness averaged over the study area for each period, highlighting the temporal differences in roughness patterns. The spring map shows some rough regions such as the Arctic Ocean north of the Canadian Arctic Archipelago and the

Fram Strait east of Greenland. The Fram Strait is an important gateway to exporting multiyear sea ice and is one of the most dynamic regions in the Arctic Ocean, especially in spring. The seasonal change of sea ice roughness from spring to summer was also explored, showing the reduction of the surface roughness of sea ice associated with the melt processes of the sea ice during the warm season.

We also evaluated the accuracy of the MISR-derived surface roughness maps and compared them with other remote sensing data products. The results show good agreement between the MISR-derived roughness maps and Landsat 8 and Sentinel-1 images for the studied regions. We also identified regions of high sea ice roughness and investigated the seasonal changes in sea ice roughness values. A preliminary exploration of spatial and seasonal changes in sea ice roughness for two locations shows the ability of our method to characterize the roughness of different ice types.

In this study, we showed that the developed image processing system and its data products can help the sea ice research community to gain insights into the seasonal and interannual changes in sea ice roughness over the Arctic. This method is the first attempt at creating Arctic-wide maps of sea ice roughness from MISR multiangular information. While there are limitations to the remote sensing technique, the study indicates that MISR data has several advantages, such as a long record of data, near-global coverage, and high spatial resolution. Overall, this appears to be a promising method for quantifying and mapping Arctic-wide sea ice surface roughness and characterizing spatial patterns and variability of sea ice surface topography and seasonal changes in sea ice roughness over an extensive area for different seasons at a horizontal scale of 275 meters. Further research is needed to

investigate the sea ice roughness patterns in other seasons and years and their implications for the Arctic climate system.

This research revealed that clouds and cloudy training data sets are likely to contribute to a significant part of the error and uncertainty in the model predictions for sea ice roughness. On the other hand, we found that the MISR cloud mask data products are not reliable in the Arctic, and their resolution of 1.1 km is not suitable for our sea ice roughness model, which requires a resolution of 275 meters. Therefore, we decided not to use any cloud mask for building the training dataset for our KNN algorithm. During the preparation of the training dataset for our KNN algorithm, we manually examined and removed several images that were visually determined to be cloudy and manually selected cloud-free images for our model. However, this approach is challenging and not accurate, and an automated cloud classifier is necessary to build a more robust training dataset. Moreover, the experiences and challenges that we faced in this research motivated us to conduct further studies to build a robust cloud detection algorithm specifically optimized for our sea ice roughness model requirements, which will contribute to the improvement of the accuracy and reliability of our model predictions. Consequently, this set the basis for our next research study.

In the second study, we developed a binary classification algorithm for identifying cloudy and clear pixels in MISR images. The MISR instrument consists of nine cameras, each with a resolution of 275 meters at the nadir and all red bands, which observe the Earth's surface from different angles. The red band values extracted from all nine cameras were used to build a training dataset for two different months, April and July. This period is identical to

the period we developed our sea ice roughness model. To ensure accuracy, the labeled pixels were first visually assessed and then divided into training and test datasets, with 70% of the data used for training and 30% for testing. The samples were selected from different MISR paths covering various regions in the Arctic. We trained a neural network algorithm on the training dataset and tested various architectures and hyperparameters to find the best performance for each season. The performance of the binary classification algorithm was evaluated using confusion matrices and performance statistics, which were compared to visual assessment.

Detecting clouds over sea ice is a hard problem and this work is an example of how machine learning can contribute to this hard problem. In this research, machine learning allowed for the use of a different method for cloud detection that is not dependent on thresholding. The results suggest that the binary classification algorithm using a neural network approach showed promising results in terms of accuracy and resolution in classifying pixels into cloudy and clear categories specifically over sea ice in the Arctic in MISR images. One of the advantages of this approach is that the accuracy of the algorithm is not dependent on threshold- and rule-based techniques, which makes it more flexible and efficient to generalize to new and unseen data without recalibration or adjustment of threshold values for each new image. Additionally, this approach is more flexible, efficient, and quicker to process a large amount of data. The developed algorithm provides a significant advantage over existing MISR cloud mask products such as SDCM and ASCM in terms of accuracy and spatial resolution, with a resolution of 275 meters. This is an important advancement for remote sensing applications, particularly in the Arctic where

cloud detection over sea ice has been a challenge. However, limitations include the algorithm's dependence on a dataset extracted from red band values of nine different cameras for only two months, making it uncertain how the algorithm will perform on data from different regions or during different seasons. The Precision, Recall, and F-score metrics showed good accuracy for clear pixels, but the algorithm had more difficulty with cloudy pixels. Also, this method only distinguishes between two classes and does not provide cloud detection confidence estimates, which is a limitation compared to SDCM and ASCM which differentiate between more classes. Overall, this study provides a foundation and potential for further refinement and extension of the algorithm for cloud detection in remote sensing applications.

This research has demonstrated the value of multiangular data for mapping Arctic sea ice and clouds and future work could extend this effort to the Antarctic region. It would also be valuable to combine radar data with multiangular optical data to extend measurements beyond the sunlit season. Future work could also use the time series of MISR data (2000-present) to explore trends in sea ice roughness and clouds over both the Arctic and Antarctic, both of which are changing in response to climate change.

This research has also shown how machine learning can improve our ability to characterize sea ice and detect clouds. The combination of multiangular data and machine learning holds great promise for improving our mapping and understanding of snow and ice.

References

- Andreas, E.L., Horst, T.W., Grachev, A.A., Persson, P.O.G., Fairall, C.W., Guest, P.S., Jordan, R.E., 2010. Parametrizing turbulent exchange over summer sea ice and the marginal ice zone. *Quarterly Journal of the Royal Meteorological Society* 136, 927–943. <https://doi.org/10.1002/qj.618>
- Arya, S., 1973. Contribution of form drag on pressure ridges to the air stress on Arctic ice. <https://doi.org/10.1029/JC078I030P07092>
- Arya, S.P.S., 1975. A drag partition theory for determining the large-scale roughness parameter and wind stress on the Arctic pack ice. *Journal of Geophysical Research (1896-1977)* 80, 3447–3454. <https://doi.org/10.1029/JC080i024p03447>
- Beckers, J.F., Renner, A.H.H., Spreen, G., Gerland, S., Haas, C., 2015. Sea-ice surface roughness estimates from airborne laser scanner and laser altimeter observations in Fram Strait and north of Svalbard. *Annals of Glaciology* 56, 235–244. <https://doi.org/10.3189/2015AoG69A717>
- Brunt, K.M., Hawley, R.L., Lutz, E.R., Studinger, M., Sonntag, J.G., Hofton, M.A., Andrews, L.C., Neumann, T.A., 2017. Assessment of NASA airborne laser altimetry data using ground-based GPS data near Summit Station, Greenland. *The Cryosphere* 11, 681–692. <https://doi.org/10.5194/tc-11-681-2017>
- Castellani, G., Lüpkes, C., Hendricks, S., Gerdes, R., 2014. Variability of Arctic sea-ice topography and its impact on the atmospheric surface drag. *Journal of Geophysical Research: Oceans* 119, 6743–6762. <https://doi.org/10.1002/2013JC009712>
- Cavalieri, D.J., Parkinson, C.L., Gloersen, P., Comiso, J.C., Zwally, H.J., 1999. Deriving long-term time series of sea ice cover from satellite passive-microwave multisensor data sets. *Journal of Geophysical Research: Oceans* 104, 15803–15814. <https://doi.org/10.1029/1999JC900081>
- Chen, N., Li, W., Gatebe, C., Tanikawa, T., Hori, M., Shimada, R., Aoki, T., Stamnes, K., 2018. New neural network cloud mask algorithm based on radiative transfer simulations. *Remote Sensing of Environment* 219, 62–71. <https://doi.org/10.1016/j.rse.2018.09.029>
- Comiso, J.C., 2002. A rapidly declining perennial sea ice cover in the Arctic. *Geophysical Research Letters* 29, 17-1-17–4. <https://doi.org/10.1029/2002GL015650>
- Comiso, J.C., 1991. Satellite remote sensing of the Polar Oceans. *Journal of Marine Systems* 2, 395–434. [https://doi.org/10.1016/0924-7963\(91\)90044-U](https://doi.org/10.1016/0924-7963(91)90044-U)
- Comiso, J.C., Parkinson, C.L., Gersten, R., Stock, L., 2008. Accelerated decline in the Arctic sea ice cover. *Geophysical Research Letters* 35. <https://doi.org/10.1029/2007GL031972>
- Di Girolamo, L., Davies, R., 1994. A band-differenced angular signature technique for cirrus cloud detection. *IEEE Transactions on Geoscience and Remote Sensing* 32, 890–896. <https://doi.org/10.1109/36.298017>
- Di Girolamo, L., Wilson, M.J., 2003. A first look at band-differenced angular signatures for cloud detection from MISR. *IEEE Transactions on Geoscience and Remote Sensing* 41, 1730–1734. <https://doi.org/10.1109/TGRS.2003.815659>
- Diner, D.J., 2013. MISR Level 1B2 Ellipsoid Data (MI1B2E_V1).

- Diner, D.J., Asner, G.P., Davies, R., Knyazikhin, Y., Muller, J.-P., Nolin, A.W., Pinty, B., Schaaf, C.B., Stroeve, J., 1999a. New Directions in Earth Observing: Scientific Applications of Multiangle Remote Sensing. *Bulletin of the American Meteorological Society* 80, 2209–2228. [https://doi.org/10.1175/1520-0477\(1999\)080<2209:NDIEOS>2.0.CO;2](https://doi.org/10.1175/1520-0477(1999)080<2209:NDIEOS>2.0.CO;2)
- Diner, D.J., Beckert, J.C., Reilly, T.H., Bruegge, C.J., Conel, J.E., Kahn, R.A., Martonchik, J.V., Ackerman, T.P., Davies, R., Gerstl, S.A.W., Gordon, H.R., Muller, J.-P., Myneni, R.B., Sellers, P.J., Pinty, B., Verstraete, M.M., 1998. Multi-angle Imaging SpectroRadiometer (MISR) instrument description and experiment overview. *IEEE Transactions on Geoscience and Remote Sensing* 36, 1072–1087. <https://doi.org/10.1109/36.700992>
- Diner, D.J., Braswell, B.H., Davies, R., Gobron, N., Hu, J., Jin, Y., Kahn, R.A., Knyazikhin, Y., Loeb, N., Muller, J.-P., Nolin, A.W., Pinty, B., Schaaf, C.B., Seiz, G., Stroeve, J., 2005. The value of multiangle measurements for retrieving structurally and radiatively consistent properties of clouds, aerosols, and surfaces. *Remote Sensing of Environment* 97, 495–518. <https://doi.org/10.1016/j.rse.2005.06.006>
- Diner, D.J., Davies, R., Di Girolamo, L., Horvath, A., Moroney, C., Muller, J.-P., Paradise, S.R., Wenkert, D., Zong, J., 1999b. MISR Level 2 Cloud Detection and Classification Algorithm Theoretical Basis.
- Diner, D.J., Di Girolamo, L., Clothiaux, E.E., 1999c. MISR Level 1 Cloud Detection Algorithm Theoretical Basis.
- Eicken, H., Grenfell, T.C., Perovich, D.K., Richter-Menge, J.A., Frey, K., 2004. Hydraulic controls of summer Arctic pack ice albedo. *Journal of Geophysical Research: Oceans* 109. <https://doi.org/10.1029/2003JC001989>
- Elvidge, A.D., Renfrew, I.A., Weiss, A.I., Brooks, I.M., Lachlan-Cope, T.A., King, J.C., 2015. Observations of surface momentum exchange over the marginal-ice-zone and recommendations for its parameterization (preprint). *Dynamics/Field Measurements/Troposphere/Physics (physical properties and processes)*. <https://doi.org/10.5194/acpd-15-26609-2015>
- Farrell, S.L., Duncan, K., Buckley, E.M., Richter-Menge, J., Li, R., 2020. Mapping Sea Ice Surface Topography in High Fidelity With ICESat-2. *Geophysical Research Letters* 47, e2020GL090708. <https://doi.org/10.1029/2020GL090708>
- Fetterer, F., Untersteiner, N., 1998. Observations of melt ponds on Arctic sea ice. *Journal of Geophysical Research: Oceans* 103, 24821–24835. <https://doi.org/10.1029/98JC02034>
- Garay, M.J., Mazzoni, D., Davies, R., Diner, D.J., 2005. The application of support vector machines to analysis of global satellite data sets from MISR. Presented at the Fourth Conference on Artificial Intelligence, San Diego, CA.
- Genkova, I., Wilson, M., Yang, Y., Zhao, G., Chapman, B., Snodgrass, E., Mazzoni, D., Girolamo, L., 2005. The synergy of the MISR cloud masks for global cloud climatology. *Proc SPIE*. <https://doi.org/10.1117/12.627909>
- Guest, P.S., Davidson, K.L., 1991. The aerodynamic roughness of different types of sea ice. *Journal of Geophysical Research: Oceans* 96, 4709–4721. <https://doi.org/10.1029/90JC02261>

- Gupta, M., Barber, D.G., Scharien, R.K., Isleifson, D., 2014. Detection and classification of surface roughness in an Arctic marginal sea ice zone. *Hydrological Processes* 28, 599–609. <https://doi.org/10.1002/hyp.9593>
- Holland, M.M., Bitz, C.M., Tremblay, B., 2006. Future abrupt reductions in the summer Arctic sea ice. *Geophysical Research Letters* 33. <https://doi.org/10.1029/2006GL028024>
- Hughes, M.J., Kennedy, R., 2019. High-Quality Cloud Masking of Landsat 8 Imagery Using Convolutional Neural Networks. *Remote Sensing* 11, 2591. <https://doi.org/10.3390/rs11212591>
- Kharbouche, S., Muller, J.-P., 2019. Sea Ice Albedo from MISR and MODIS: Production, Validation, and Trend Analysis. *Remote Sensing* 11, 9. <https://doi.org/10.3390/rs11010009>
- Kumar, A., Yadav, J., Mohan, R., 2020. Global warming leading to alarming recession of the Arctic sea-ice cover: Insights from remote sensing observations and model reanalysis. *Heliyon* 6, e04355. <https://doi.org/10.1016/j.heliyon.2020.e04355>
- Kwok, R., 2015. Sea ice convergence along the Arctic coasts of Greenland and the Canadian Arctic Archipelago: Variability and extremes (1992–2014). *Geophysical Research Letters* 42, 7598–7605. <https://doi.org/10.1002/2015GL065462>
- Kwok, R., Cunningham, G.F., Wensnahan, M., Rigor, I., Zwally, H.J., Yi, D., 2009. Thinning and volume loss of the Arctic Ocean sea ice cover: 2003–2008. *Journal of Geophysical Research: Oceans* 114. <https://doi.org/10.1029/2009JC005312>
- Kwok, R., Kacimi, S., Webster, M. a., Kurtz, N. t., Petty, A. a., 2020. Arctic Snow Depth and Sea Ice Thickness From ICESat-2 and CryoSat-2 Freeboards: A First Examination. *Journal of Geophysical Research: Oceans* 125, e2019JC016008. <https://doi.org/10.1029/2019JC016008>
- Kwok, R., Rothrock, D.A., 2009. Decline in Arctic sea ice thickness from submarine and ICESat records: 1958–2008. *Geophysical Research Letters* 36. <https://doi.org/10.1029/2009GL039035>
- Kwok, R., Schweiger, A., Rothrock, D.A., Pang, S., Kottmeier, C., 1998. Sea ice motion from satellite passive microwave imagery assessed with ERS SAR and buoy motions. *Journal of Geophysical Research: Oceans* 103, 8191–8214. <https://doi.org/10.1029/97JC03334>
- Landy, J.C., Ehn, J.K., Barber, D.G., 2015. Albedo feedback enhanced by smoother Arctic sea ice. *Geophysical Research Letters* 42, 10,714–10,720. <https://doi.org/10.1002/2015GL066712>
- Lei, R., Tian-Kunze, X., Leppäranta, M., Wang, J., Kaleschke, L., Zhang, Z., 2016. Changes in summer sea ice, albedo, and partitioning of surface solar radiation in the Pacific sector of Arctic Ocean during 1982–2009. *Journal of Geophysical Research: Oceans* 121, 5470–5486. <https://doi.org/10.1002/2016JC011831>
- Lindsay, R.W., Zhang, J., 2005. The Thinning of Arctic Sea Ice, 1988–2003: Have We Passed a Tipping Point? *Journal of Climate* 18, 4879–4894. <https://doi.org/10.1175/JCLI3587.1>
- Lüpkes, C., Gryanik, V.M., Hartmann, J., Andreas, E.L., 2012. A parametrization, based on sea ice morphology, of the neutral atmospheric drag coefficients for weather

- prediction and climate models. *Journal of Geophysical Research: Atmospheres* 117. <https://doi.org/10.1029/2012JD017630>
- Lüpkes, C., Gryanik, V.M., Rösel, A., Birnbaum, G., Kaleschke, L., 2013. Effect of sea ice morphology during Arctic summer on atmospheric drag coefficients used in climate models. *Geophysical Research Letters* 40, 446–451. <https://doi.org/10.1002/grl.50081>
- Lynnes, C., Huang, T., 2022. Future of Big Earth Data Analytics, in: Huang, T., Vance, T.C., Lynnes, C. (Eds.), *Special Publications*. Wiley, pp. 293–305. <https://doi.org/10.1002/9781119467557.ch17>
- Mazzoni, D., Garay, M.J., Davies, R., Nelson, D., 2007. An operational MISR pixel classifier using support vector machines. *Remote Sensing of Environment, Multi-angle Imaging SpectroRadiometer (MISR) Special Issue* 107, 149–158. <https://doi.org/10.1016/j.rse.2006.06.021>
- Meier, W.N., Hovelsrud, G.K., van Oort, B.E.H., Key, J.R., Kovacs, K.M., Michel, C., Haas, C., Granskog, M.A., Gerland, S., Perovich, D.K., Makshtas, A., Reist, J.D., 2014. Arctic sea ice in transformation: A review of recent observed changes and impacts on biology and human activity. *Reviews of Geophysics* 52, 185–217. <https://doi.org/10.1002/2013RG000431>
- Meier, W.N., Stroeve, J., Fetterer, F., 2007. Whither Arctic sea ice? A clear signal of decline regionally, seasonally and extending beyond the satellite record. *Annals of Glaciology* 46, 428–434. <https://doi.org/10.3189/172756407782871170>
- Min, C., Mu, L., Yang, Q., Ricker, R., Shi, Q., Han, B., Wu, R., Liu, J., 2019. Sea ice export through the Fram Strait derived from a combined model and satellite data set. *The Cryosphere* 13, 3209–3224. <https://doi.org/10.5194/tc-13-3209-2019>
- Morassutti, M.P., Ledrew, E.F., 1996. Albedo and Depth of Melt Ponds on Sea-Ice. *International Journal of Climatology* 16, 817–838. [https://doi.org/10.1002/\(SICI\)1097-0088\(199607\)16:7<817::AID-JOC44>3.0.CO;2-5](https://doi.org/10.1002/(SICI)1097-0088(199607)16:7<817::AID-JOC44>3.0.CO;2-5)
- Moritz, R.E., Bitz, C.M., Steig, E.J., 2002. Dynamics of recent climate change in the Arctic. *Science* 297, 1497–1502. <https://doi.org/10.1126/science.1076522>
- Mosadegh, E., Nolin, A., 2021. A Deep Learning Architecture For Mapping Arctic Sea Ice Roughness from MISR Images Based On Multi-Feature Fusion 2021, C35H-0968.
- Mosadegh, E., Nolin, A.W., 2022. A New Data Processing System for Generating Sea Ice Surface Roughness Products from the Multi-Angle Imaging SpectroRadiometer (MISR) Imagery. *Remote Sensing* 14, 4979. <https://doi.org/10.3390/rs14194979>
- Mosadegh, E., Nolin, A.W., 2020. Estimating Arctic sea ice surface roughness by using back propagation neural network 2020, C014-0005.
- Mueller, B.L., Gillett, N.P., Monahan, A.H., Zwiers, F.W., 2018. Attribution of Arctic Sea Ice Decline from 1953 to 2012 to Influences from Natural, Greenhouse Gas, and Anthropogenic Aerosol Forcing. *Journal of Climate* 31, 7771–7787. <https://doi.org/10.1175/JCLI-D-17-0552.1>
- Nolin, A.W., 2004. Towards retrieval of forest cover density over snow from the Multi-angle Imaging SpectroRadiometer (MISR). *Hydrological Processes* 18, 3623–3636. <https://doi.org/10.1002/hyp.5803>

- Nolin, A.W., Fetterer, F.M., Scambos, T.A., 2002. Surface roughness characterizations of sea ice and ice sheets: case studies with MISR data. *IEEE Transactions on Geoscience and Remote Sensing* 40, 1605–1615.
<https://doi.org/10.1109/TGRS.2002.801581>
- Nolin, A.W., Mar, E., 2019. Arctic Sea Ice Surface Roughness Estimated from Multi-Angular Reflectance Satellite Imagery. *Remote Sensing* 11, 50.
<https://doi.org/10.3390/rs11010050>
- Nolin, A.W., Payne, M.C., 2007. Classification of glacier zones in western Greenland using albedo and surface roughness from the Multi-angle Imaging SpectroRadiometer (MISR). *Remote Sensing of Environment, Multi-angle Imaging SpectroRadiometer (MISR) Special Issue* 107, 264–275.
<https://doi.org/10.1016/j.rse.2006.11.004>
- Notz, D., Community, S., 2020. Arctic Sea Ice in CMIP6. *Geophysical Research Letters* 47, e2019GL086749. <https://doi.org/10.1029/2019GL086749>
- Olson, D.L., Delen, D., 2008. *Advanced Data Mining Techniques*. Springer Science & Business Media.
- Parkinson, C.L., Cavalieri, D.J., Gloersen, P., Zwally, H.J., Comiso, J.C., 1999. Arctic sea ice extents, areas, and trends, 1978–1996. *Journal of Geophysical Research: Oceans* 104, 20837–20856. <https://doi.org/10.1029/1999JC900082>
- Perovich, D.K., Polashenski, C., 2012. Albedo evolution of seasonal Arctic sea ice: ALEDO EVOLUTION OF SEASONAL SEA ICE. *Geophys. Res. Lett.* 39, n/a-n/a. <https://doi.org/10.1029/2012GL051432>
- Peterson, I.K., Prinsenberg, S.J., Holladay, J.S., 2008. Observations of sea ice thickness, surface roughness and ice motion in Amundsen Gulf. *Journal of Geophysical Research: Oceans* 113. <https://doi.org/10.1029/2007JC004456>
- Petty, A.A., Tsamados, M.C., Kurtz, N.T., 2017. Atmospheric form drag coefficients over Arctic sea ice using remotely sensed ice topography data, spring 2009–2015: ATMOSPHERIC DRAG OVER ARCTIC SEA ICE. *J. Geophys. Res. Earth Surf.* 122, 1472–1490. <https://doi.org/10.1002/2017JF004209>
- Poulsen, C., Egede, U., Robbins, D., Sandeford, B., Tazi, K., Zhu, T., 2020. Evaluation and comparison of a machine learning cloud identification algorithm for the SLSTR in polar regions. *Remote Sensing of Environment* 248, 111999.
<https://doi.org/10.1016/j.rse.2020.111999>
- Rantanen, M., Karpechko, A.Y., Lipponen, A., Nordling, K., Hyvärinen, O., Ruosteenoja, K., Vihma, T., Laaksonen, A., 2022. The Arctic has warmed nearly four times faster than the globe since 1979. *Commun Earth Environ* 3, 1–10.
<https://doi.org/10.1038/s43247-022-00498-3>
- Riggs, G., Hall, D.K., n.d. Reduction of Cloud Obscuration in the MODIS Snow Data Product 8.
- Sea Ice Glossary - Woods Hole Oceanographic Institution, n.d. . <https://www.whoi.edu/>. URL <https://www.whoi.edu/know-your-ocean/ocean-topics/how-the-ocean-works/frozen-ocean/sea-ice/sea-ice-glossary/> (accessed 8.12.22).
- Segal, R.A., Scharien, R.K., Cafarella, S., Tedstone, A., 2020. Characterizing winter landfast sea-ice surface roughness in the Canadian Arctic Archipelago using Sentinel-1 synthetic aperture radar and the Multi-angle Imaging

- SpectroRadiometer. *Annals of Glaciology* 61, 284–298.
<https://doi.org/10.1017/aog.2020.48>
- Serreze, M.C., Maslanik, J.A., Scambos, T.A., Fetterer, F., Stroeve, J., Knowles, K., Fowler, C., Drobot, S., Barry, R.G., Haran, T.M., 2003. A record minimum arctic sea ice extent and area in 2002. *Geophysical Research Letters* 30.
<https://doi.org/10.1029/2002GL016406>
- Shi, T., Clothiaux, E.E., Yu, B., Braverman, A.J., Groff, D.N., 2007. Detection of daytime arctic clouds using MISR and MODIS data. *Remote Sensing of Environment* 107, 172–184. <https://doi.org/10.1016/j.rse.2006.10.015>
- Shi, T., Yu, B., Clothiaux, E.E., Braverman, A.J., 2008. Daytime Arctic Cloud Detection Based on Multi-Angle Satellite Data with Case Studies. *Journal of the American Statistical Association* 103, 584–593.
- Shi, T., Yu, B., Clothiaux, E.E., Braverman, A.J., 2004. Cloud Detection over Snow and Ice Using MISR Data.
- Steiner, N., Harder, M., Lemke, P., 1999. Sea-ice roughness and drag coefficients in a dynamic–thermodynamic sea-ice model for the Arctic. *Tellus A: Dynamic Meteorology and Oceanography* 51, 964–978.
<https://doi.org/10.3402/tellusa.v51i5.14505>
- Stillinger, T., Roberts, D.A., Collar, N.M., Dozier, J., 2019. Cloud Masking for Landsat 8 and MODIS Terra Over Snow-Covered Terrain: Error Analysis and Spectral Similarity Between Snow and Cloud. *Water Resources Research* 55, 6169–6184.
<https://doi.org/10.1029/2019WR024932>
- Stowe, L.L., Davis, P.A., McClain, E.P., 1999. Scientific Basis and Initial Evaluation of the CLAVR-1 Global Clear/Cloud Classification Algorithm for the Advanced Very High Resolution Radiometer. *Journal of Atmospheric and Oceanic Technology* 16, 656–681. [https://doi.org/10.1175/1520-0426\(1999\)016<0656:SBAIEO>2.0.CO;2](https://doi.org/10.1175/1520-0426(1999)016<0656:SBAIEO>2.0.CO;2)
- Stroeve, J., Notz, D., 2018. Changing state of Arctic sea ice across all seasons. *Environ. Res. Lett.* 13, 103001. <https://doi.org/10.1088/1748-9326/aade56>
- Stroeve, J., Notz, D., 2015. Insights on past and future sea-ice evolution from combining observations and models. *Global and Planetary Change* 135, 119–132.
<https://doi.org/10.1016/j.gloplacha.2015.10.011>
- Stroeve, J.C., Kattsov, V., Barrett, A., Serreze, M., Pavlova, T., Holland, M., Meier, W.N., 2012. Trends in Arctic sea ice extent from CMIP5, CMIP3 and observations. *Geophysical Research Letters* 39. <https://doi.org/10.1029/2012GL052676>
- Stroeve, J.C., Nolin, A.W., 2002. New methods to infer snow albedo from the MISR instrument with applications to the Greenland ice sheet. *IEEE Transactions on Geoscience and Remote Sensing* 40, 1616–1625.
<https://doi.org/10.1109/TGRS.2002.801144>
- Studinger, M., n.d. IceBridge ATM L2 Icessn Elevation, Slope, and Roughness, Version 2. Boulder, Colorado USA. NASA National Snow and Ice Data Center Distributed Active Archive Center. <https://doi.org/10.5067/CPRXXK3F39RV> (accessed on 1 June 2018).

- Teleti, P.R., Luis, A.J., 2013. Sea Ice Observations in Polar Regions: Evolution of Technologies in Remote Sensing. *International Journal of Geosciences* 4, 1031–1050. <https://doi.org/10.4236/ijg.2013.47097>
- van Tiggelen, M., Smeets, P.C.J.P., Reijmer, C.H., Wouters, B., Steiner, J.F., Nieuwstraten, E.J., Immerzeel, W.W., van den Broeke, M.R., 2021. Mapping the aerodynamic roughness of the Greenland ice sheets surface using ICESat-2: Evaluation over the K-transect (preprint). *Ice sheets/Atmospheric Interactions*. <https://doi.org/10.5194/tc-2020-378>
- Von Saldern, C., Busche, T., Haas, C., Dierking, W., 2005. Analysis of sea ice surface roughness and thickness profiles for improvement of SAR ice type classification, in: European Space Agency, (Special Publication) ESA SP. Presented at the Proceedings of the 2004 Envisat & ERS Symposium, 6-10 Sept.2004, Salzburg, Austria. European Space Agency. Compiled by H. Lacoste and L. Ouwehand. SP-572, pp. 2159–2164.
- Walker, N.P., Partington, K.C., Van Woert, M.L., Street, T.L.T., 2006. Arctic Sea Ice Type and Concentration Mapping Using Passive and Active Microwave Sensors. *IEEE Transactions on Geoscience and Remote Sensing* 44, 3574–3584. <https://doi.org/10.1109/TGRS.2006.881116>
- White, C.H., Heidinger, A.K., Ackerman, S.A., 2021. Evaluation of Visible Infrared Imaging Radiometer Suite (VIIRS) neural network cloud detection against current operational cloud masks. *Atmospheric Measurement Techniques* 14, 3371–3394. <https://doi.org/10.5194/amt-14-3371-2021>
- Yi, D., Zwally, H.J., Sun, X., 2005. ICESat measurement of Greenland ice sheet surface slope and roughness. *Annals of Glaciology* 42, 83–89. <https://doi.org/10.3189/172756405781812691>
- Zekoll, V., Main-Knorn, M., Alonso, K., Louis, J., Frantz, D., Richter, R., Pflug, B., 2021. Comparison of Masking Algorithms for Sentinel-2 Imagery. *Remote Sensing* 13, 137. <https://doi.org/10.3390/rs13010137>
- Zhang, J., Rothrock, D., Steele, M., 2000. Recent Changes in Arctic Sea Ice: The Interplay between Ice Dynamics and Thermodynamics. *Journal of Climate* 13, 3099–3114. [https://doi.org/10.1175/1520-0442\(2000\)013<3099:RCIASI>2.0.CO;2](https://doi.org/10.1175/1520-0442(2000)013<3099:RCIASI>2.0.CO;2)
- Zhu, X.X., Tuia, D., Mou, L., Xia, G.-S., Zhang, L., Xu, F., Fraundorfer, F., 2017. Deep Learning in Remote Sensing: A Comprehensive Review and List of Resources. *IEEE Geoscience and Remote Sensing Magazine* 5, 8–36. <https://doi.org/10.1109/MGRS.2017.2762307>